The Structural and Electrochemical Properties of CuCoO₂ Crystalline Nanopowders and Thin Films: Conductivity Experimental Analysis and Insights from Density Functional Theory Calculations

Hasnae Chfii [1], Amal Bouich [1,2] , Andreu Andrio [3] , Joeluis Cerutti Torres [2,4], Bernabé Mari Soucase [1] ,
Pablo Palacios [2,4] , Mohammed Abd Lefdil [5] and Vicente Compañ [6,*]

1   Escuela Técnica Superior de Ingeniería del Diseño, Universitat Politècnica de València, 46022 València, Spain;
    bmari@fis.upv.es (B.M.S.)
2   Instituto de Energía Solar, ETSI Telecomunicación, Universidad Politécnica de Madrid, Ciudad Universitaria,
    28040 Madrid, Spain; pablo.palacios@upm.es (P.P.)
3   Departamento de Física, Universitat Jaume I, 12080 Castellón de la Plana, Spain; andrio@uji.es
4   Departamento Física Aplicada a las Ingenierías Aeronáutica y Naval, ETSI Aeronáutica y del Espacio,
    Universidad Politécnica de Madrid, Pz. Cardenal Cisneros, 3, 28040 Madrid, Spain
5   Laboratory MANAPSE, University Mohammed V, Rabat 10100, Morocco
6   Departamento de Termodinámica Aplicada, Universitat Politècnica de Valencia, 46022 Valencia, Spain
*   Correspondence: vicommo@ter.upv.es

Abstract: A novel manufacturing process is presented for producing nanopowders and thin films of CuCoO₂ (CCO) material. This process utilizes three cost-effective synthesis methods: hydrothermal, sol-gel, and solid-state reactions. The resulting delafossite CuCoO₂ samples were deposited onto transparent substrates through spray pyrolysis, forming innovative thin films with a nanocrystal powder structure. Prior to the transformation into thin films, CuCoO₂ powder was first produced using a low-cost approach. The precursors for both powders and thin films were deposited onto glass surfaces using a spray pyrolysis process, and their characteristics were examined through X-ray diffraction, scanning electron microscopy, HR-TEM, UV-visible spectrophotometry, and electrochemical impedance spectroscopy (EIS) analyses were conducted to determine the conductivity in the transversal direction of this groundbreaking material for solar cell applications. On the other hand, the sheet resistance of the samples was investigated using the four-probe method to obtain the sheet resistivity and then calculate the in-plane conductivity of the samples. We also investigated the aging characteristics of different precursors with varying durations. The functional properties of CuCoO₂ samples were explored by studying chelating agent and precursor solution aging periods using Density Functional Theory calculations (DFT). A complementary Density Functional Theory study was also performed in order to evaluate the electronic structure of this compound. Resuming, this study thoroughly discusses the synthesis of delafossite powders and their conversion into thin films, which hold potential as hole transport layers in transparent optoelectronic devices.

Keywords: delafossite; powder; films; spray pyrolysis; EIS; conductivity; relaxation time

1. Introduction

In recent decades, there has been a significant demand for advancements in the integration of high-efficiency p-type transparent conductive oxides (TCOs) into industrial applications, particularly in the past few decades [1–5]. However, the research community is keen on exploring alternative TCOs and enhancing their electrical and optical properties to improve device efficiency [6–8]. Among various delafossite oxides, copper-based delafossite oxides stand out as promising candidates due to their desirable electrical and optical characteristics. The copper-based delafossite oxide, specifically CuMO₂ (where M

represents Al, Ga, Fe, Co, Mg, Fe, Cr. . .), has attracted considerable attention for diverse applications such as batteries [9–15], luminescent materials [16–21], thermoelectrics [22–28], solar energy conversion and photocatalysis [29–35], hydrogen production through water splitting using photocathodes [36–41], and gas sensors [42–49]. In this study, we focus on the $CuCoO_2$ compound, in view of intriguing structural, optical, and electrical properties; it has only been studied in a limited number of publications, and in most of them, the $CuCoO_2$ compound has shown interesting properties to be treated as a possible material in photovoltaic solar cells [50–58]. Extensive studies on delafossite powders and thin films reveal that $CuCoO_2$ is a p-type semiconductor that crystallizes in two distinct structures: rhombohedral (3R) [59–61] and hexagonal (2H) [60,62,63]. The successful synthesis of the $CuCoO_2$ phase has been reported in only a few papers to date. Moreover, various efforts have been made to manipulate the properties of $CuCoO_2$, such as characterizing it using different printing techniques or exploring its physical and chemical properties through doping processes involving a wide range of elements [64–67]. Considerable attention has been devoted to the integration of this delafossite material into various domains using different methodologies. Beekman et al. published a study on the synthesis of undoped delafossite through ion exchange [59], while Z. Du et al. synthesized it as an electrocatalyst for the oxygen reaction [54,57] and also investigated the solvothermal synthesis of $CuCoO_2$ [57,65]. Isacfranklin et al. focused on $CuCoO_2$ electrodes for supercapacitor applications [65], whereas D. Xiong et al. conducted a study on the polyvinylpyrrolidone-assisted hydrothermal synthesis of $CuCoO_2$ [67]. Other researchers explored hydrogen-related aspects, such as J. Ding et al., who investigated Co_3O_4-$CuCoO_2$ composites [68].

Several studies have reported on the effects of Ca^{+2} doping in $CuCoO_2$. Z. Du et al. studied the optical and electrical properties of the material [57,64,67], while M. Yang et al. examined the impact of nickel doping on the structure and morphology of delafossite [58]. Limited research has been conducted on the transformation of delafossite powder into thin films [52,56,58]. Specifically, there is currently a lack of research projects focusing on the structural and electrochemical properties of $CuCoO_2$ crystalline nanopowders and thin films when they are deposited on glass substrates.

Several physical and chemical processes, such as spray pyrolysis [53,69–72] and spin-coating [73–76], have been employed to fabricate thin films of $CuCoO_2$. However, previous attempts to produce $CuCoO_2$ thin films have predominantly utilized complex and expensive techniques, posing significant practical limitations. Currently, only a few endeavors have focused on generating $CuCoO_2$ thin films in the hexagonal phase, particularly through chemical deposition methods. Therefore, the objective of this study is to develop a simpler and more efficient chemical synthesis using three different methods based on the utilization of $CuCoO_2$ powder, which yields an excellent, ordered crystalline mixture between two structures: rhombohedral and hexagonal with and good band gap values aiming to achieve thin films of this material. Comprehensive investigations were conducted to thoroughly analyze the optical and electrical characteristics of these thin films. In particular, studies of electrochemical impedance spectroscopy (EIS) analysis and simulation of delafossites-based solar cells where $CuCoO_2$ acting as low temperature hydrothermal (HTL) material is reported for the first time. The conductivity of samples, prepared using the three different techniques, was measured in direct current (named in-plane conductivity) using the four-point probe and alternating current (named transversal conductivity) by electrochemical impedance spectroscopy.

Additionally, Density Functional Theory was employed to provide a theoretical understanding of the role played by each element in the electronic structure, as well as to accurately determine the bandgap of the material.

2. Experimental Part

2.1. Synthesis of $CuCoO_2$ Powders

$CuCoO_2$ was produced using three different methods. The grains of copper(II) nitrate trihydrate ($Cu(NO_3)_2$, $3H_2O$; 99%) were used as the Cu^{+2} source; cobalt(II) nitrate hexahy-

drate (Co(NO$_3$)$_2$, 6H$_2$O; 98%) was used as the Co^{2+} source; and sodium hydroxide (NaOH) was obtained from Sigma–Aldrich. As a solvent, deionized water (DW) was utilized. At room temperature, all chemicals were added. The amount of each precursor was 2 mM of each of the copper and cobalt sources, 4.40 g of sodium hydroxide, and 70 mL of deionized water (DW), respectively. All of the precursors were measured and mixed in a reasonable amount of solvent for three hours. For hydrothermal synthesis: method 1 (sample named CuCoO$_2$_H), the liquid was placed in a 100 mL Teflon autoclave and autoclaved at 100 °C for 24 h; we washed the obtained solution several times with distilled water. Method 2: solid-state reaction (sample named CuCoO$_2$_SSR); stoichiometric amounts of the abovementioned powders were ground with ethanol solution (95%) for 24 h. The ground powder was calcined at 800 °C for 5 h. Method 3: sol-gel (sample named CuCoO$_2$_SG); copper(II) nitrate and cobalt(II) nitrate were mixed in ethylene glycol. The solution was agitated at room temperature for 1 h in a beaker before being dried at 150 °C for 5 h. On a heated plate with a magnetic stirrer, gelation took place until a purple color emerged. The amorphous powder was heated incrementally from 50 °C to 800 °C.

2.2. Synthesis of the CuCoO$_2$ Thin Films

The glass substrate cleaning process was performed by ultrasonically cleaning and drying the substrate. The dissolved nanocrystal precursor solution was then converted into a thin film. CuCoO$_2$/glass films were produced using spray pyrolysis technology. First, we dispersed 1 mg of CuCoO$_2$ powder in 10 mL of ethanol/water mixture and sonicated for 30 min to form homogeneous slurry. The CuCoO$_2$ slurry was then deposited on the glass film (Figure 1). The resulting film was annealed in air at 350 °C for 40 min to form a CuCoO$_2$-coupled glass film.
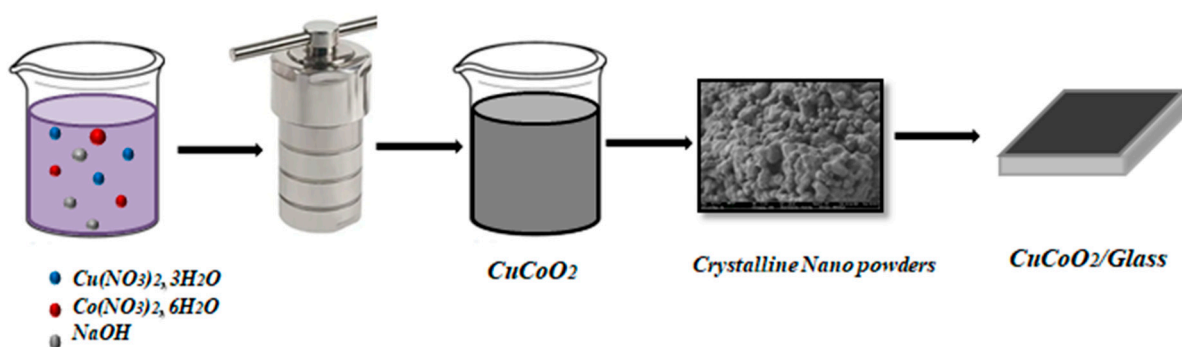

- Cu(NO$_3$)$_2$, 3H$_2$O
- Co(NO$_3$)$_2$, 6H$_2$O
- NaOH

CuCoO$_2$ Crystalline Nano powders   CuCoO$_2$/Glass

Figure 1. Schematic description of the synthesis process of the CuCoO$_2$/Glass film.

2.3. The Four-Probe Method

The measurement of conductivity in powders and polymeric thin membranes is a complex task that is influenced by various factors, including sample casting preparations, thermal/hydrothermal treatments, relative humidity, and the cell configuration used for film resistance measurements, as well as the pressure applied between the probe electrodes [77]. The four-probe method is commonly used to measure sample sheet resistance and estimate in-plane conductivity, but it may result in inaccuracies, particularly for materials with morphological anisotropy [78,79]. According to this method in which four probes are arranged equidistantly in a straight line and pushed against the film as shown in Figure 2, the resistivity may be calculated through determining the potential difference between the RE and S electrodes, due to current passing via an easily identifiable connection between the WE and CE electrodes (Figure 2). Knowing the resistivity, the sheet conductivity can be calculated from the inverse of the sheet resistivity as

$$\sigma = \frac{1}{\rho} = \frac{1}{R_s \cdot t} \qquad (1)$$

where ρ is the sheet resistivity, R_s the in-plane resistance, and t is the sheet sample thickness. In our samples, the thickness values are 140 nm, 136 nm, and 142 nm for $CuCoO_2\_H$, $CuCoO_2\_SG$, and $CuCoO_2\_SSR$, respectively.
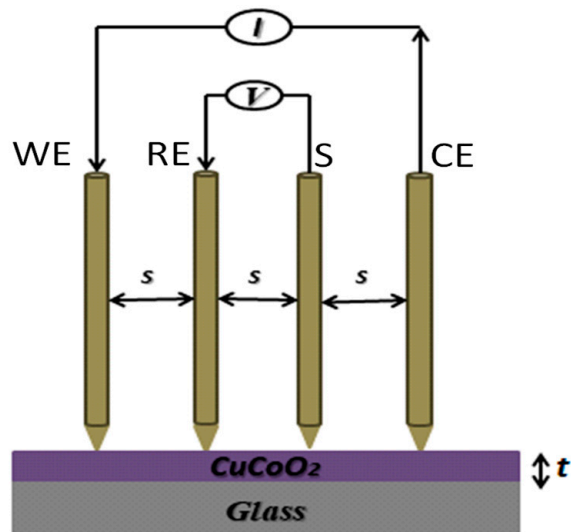

Figure 2. Schematic diagram of the four-point probe method.

2.4. Electrochemical Impedance Spectroscopy (EIS) Measurements

The conductivity was measured through the samples with a Novocontrol broadband dielectric spectrometer (BDS) equipped with an SR 830 lock-in amplifier and an Alpha dielectric interface in the frequency interval from 10^{-1} to 10^7 Hz with 0.1 V amplitude of the signal at temperatures ranging from 20 to 120 °C in increments of 20 °C. The samples were airbrushed before being tested, and their thicknesses were determined via a micrometer, averaging 10 readings from various sections of the surface. The samples were dried in a vacuum cell and placed between two gold round electrodes that served as blocking electrodes before being heated in the Novocontrol system in a neutral nitrogen-free environment. A temperature cycle from 20 to 120 °C in 20 °C increments was performed before collecting the dielectric spectra at every step to ensure uniformity and reduce interference from remaining water. During the testing, the electrodes were kept completely wet below 100 °C and replicated a 100% relative humidity environment above 100 °C in a BDS 1308 liquid device that was attached to the spectrometer and contained deionized water. To accurately control the temperature conditions, the temperature was kept constant throughout the conductivity measures (isothermal investigations) or shifted stepwise from 20 to 120 °C using a nitrogen jet (QUATRO from Novocontrol), alongside a temperature error of 0.1 K throughout each frequency sweep.

The frequency dependence of complex impedance $Z^*(\omega) = Z'(\omega) + j \cdot Z''(\omega)$ yields the real component of conductivity as

$$\sigma'(\omega) = \frac{Z'(\omega) \cdot L}{\left[(Z'(\omega))^2 + (Z''(\omega))^2\right] \cdot S} = \frac{L}{R_0 \cdot S} \tag{2}$$

where L and S represent the thickness and area of the sample in contact with the electrodes, and R_0 represents its resistance.

3. Results and Discussion

3.1. Structural Analysis

Figure 3 presents the XRD diffractograms of the as-prepared samples (a) $CuCoO_2\_H$, (b) $CuCoO_2\_SG$, and (c) $CuCoO_2\_SSR$ with a mixture of two structures: rhombohedral and hexagonal. This was confirmed by checking the databases: JCPDS Map No. 074-1855 and

JCPDS Map No. 021-0256. The three patterns observed in Figure 3 were identified as pure phases of $CuCoO_2$ without secondary phases. The main peak of delafossite $CuCoO_2$ in the rhombohedral structure (110) is at $2\theta = 37.92°$, and the hexagonal structure is at $2\theta = 38.27°$.
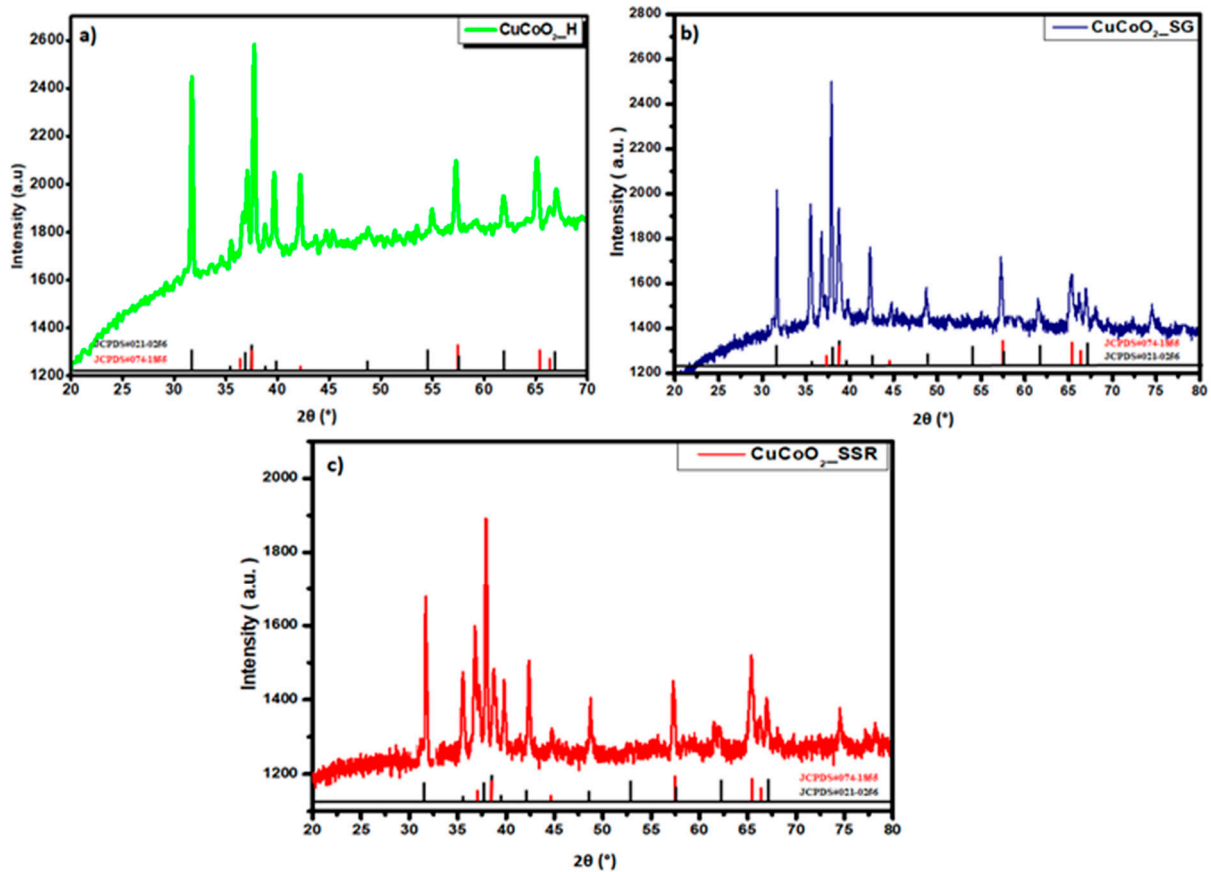

Figure 3. XRD patterns of $CuCoO_2$ nanocrystals prepared by (**a**) hydrothermal ($CuCoO_2$_H), (**b**) sol-gel ($CuCoO_2$_SG), and (**c**) solid-state reaction ($CuCoO_2$_SSR).

After characterization of $CuCoO_2$ nanoparticles prepared by three methods: the hydrothermal method, sol-gel method, and solid-state reaction method, we examined their structure following deposition onto glass substrates and thin film synthesis using spray pyrolysis. Figure 4 shows the XRD graphs of the thin films of $CuCoO_2$ on the glass substrates. We observed some of the peaks shown in the XRD pattern, which now appear in the diffractograms of the deposited film. However, the structure did not change, and the material showed two structures containing delafossite: 3R-$CuCoO_2$ (JCPDS#21-0256) and 2H-$CuCoO_2$ (JCPDS#74-1855). Furthermore, it is clear that each XRD pattern begins with a tablet. It belongs to the glass substrate.

3.2. FE-SEM Analysis

We are interested in the morphology and particle size distribution of our compound $CuCoO_2$. Observations by scanning electron microscopy (SEM) were carried out on a submicron scale on the three prepared $CuCoO_2$ nanocrystal powders as shown in Figure 5. A 1 μm magnification is given.

FE-SEM images of the powders show that the submicron $CuCoO_2$_H, $CuCoO_2$_SG, and $CuCoO_2$_SSR are in the form of a powder made up of crystals of different sizes, and they contain agglomerates of hexagonal particles and crystals like rhombohedral shapes. There have been no additional morphologies detected, which confirms the XRD results.
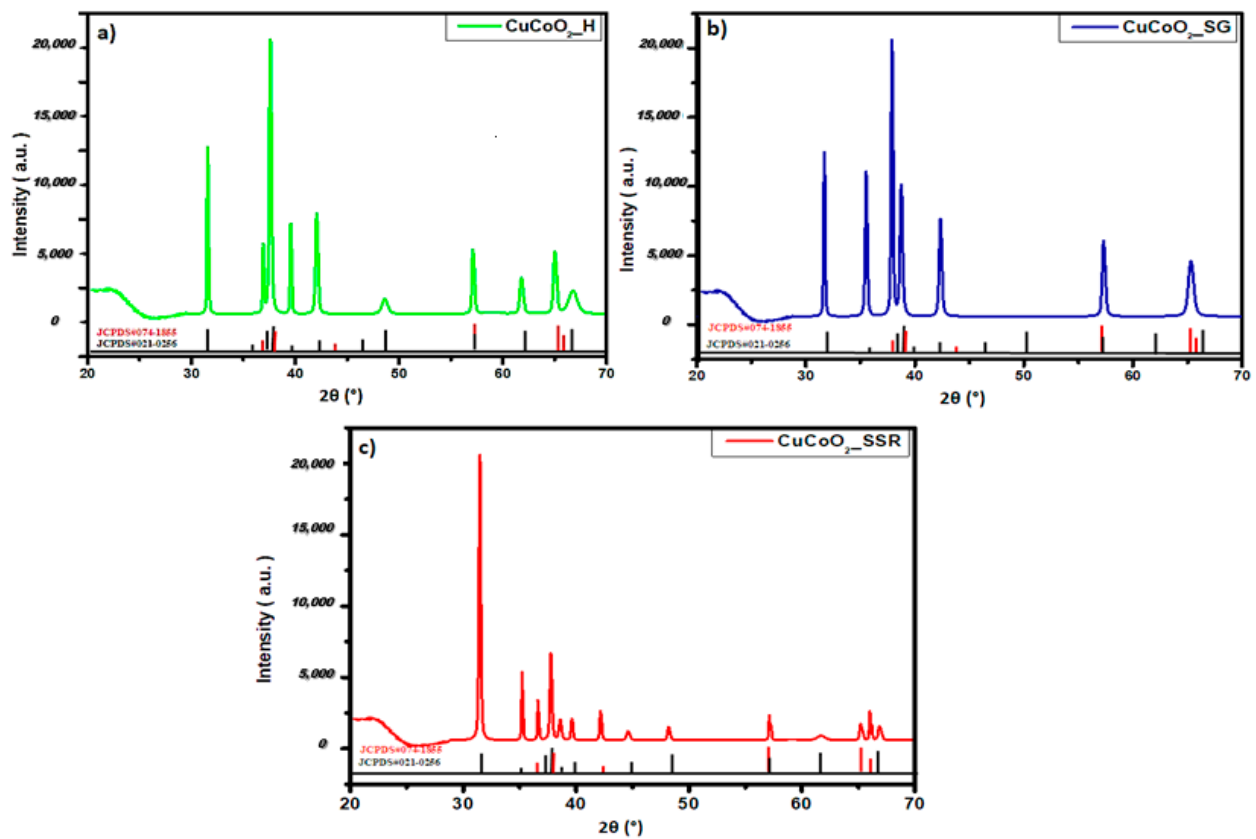
Figure 4. XRD diffractograms of films deposited on glass substrates of (**a**) CuCoO$_2$_H, (**b**) CuCoO$_2$_SG, and (**c**) CuCoO$_2$_SSR.

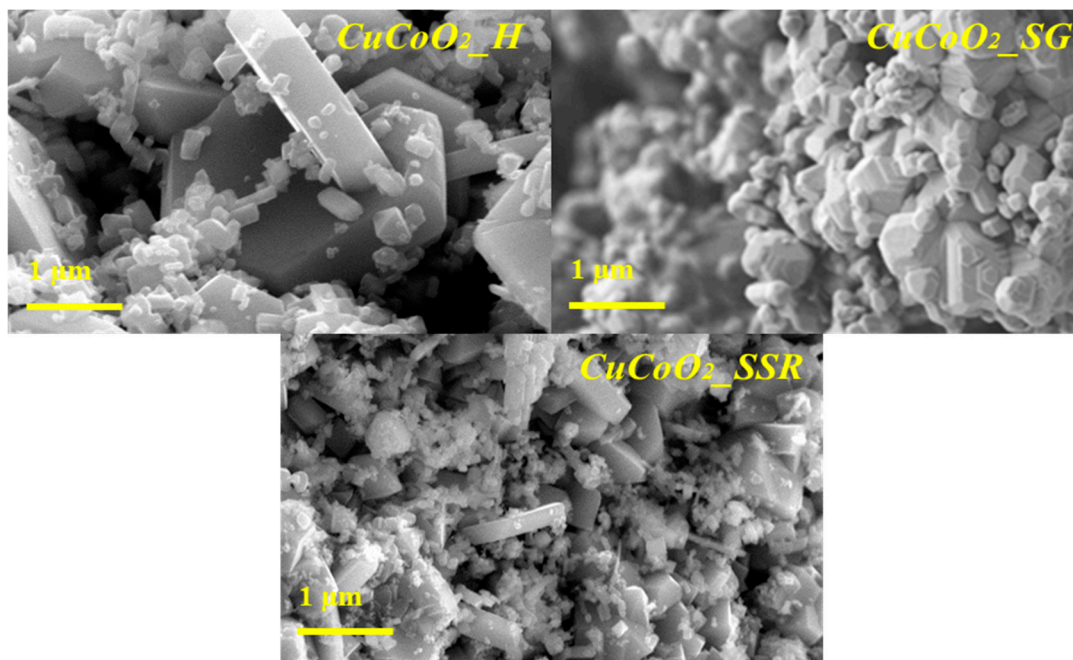**Figure 5.** FE-SEM images for the three nanocrystalline powders.

Figure 6 shows FE-SEM images of produced thin films comprising CuCoO$_2$_H, CuCoO$_2$_SG, and CuCoO$_2$_SSR at 1 μm. After deposition with the spray pyrolysis technique, all films had a uniform distribution of nanocrystalline particles.
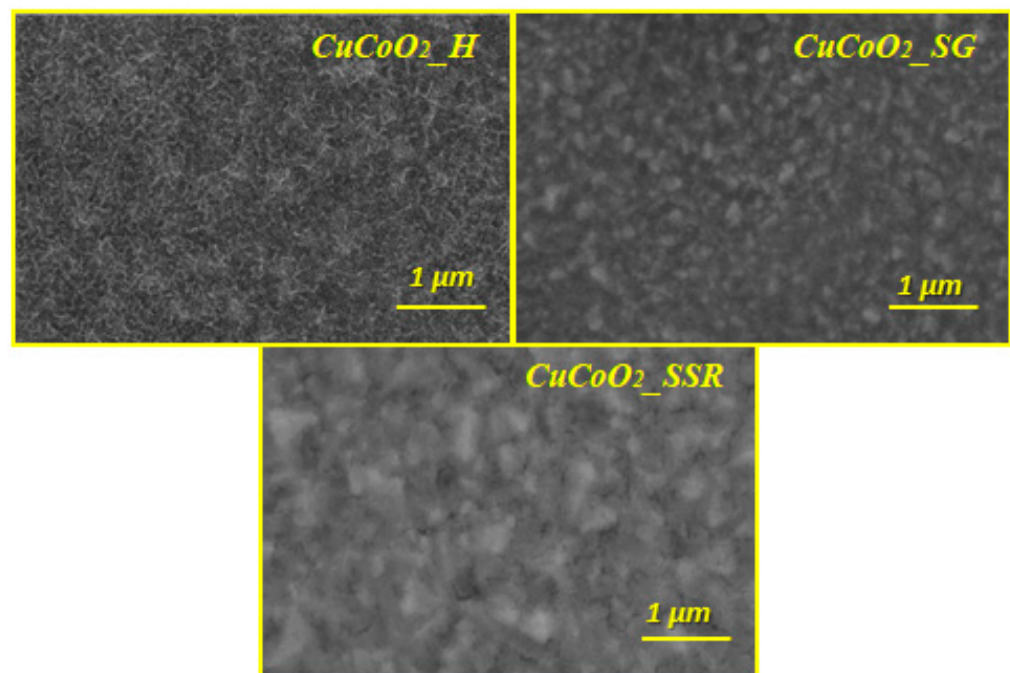
Figure 6. FE-SEM images for CuCoO$_2$_H, CuCoO$_2$_SG, and CuCoO$_2$_SSR films at 1 μm.

3.3. HR-TEM

Analysis

Figure 7 shows the characterization of the three samples with transmission electron microscope (TEM) characterization, and the high-resolution transmission electron microscopy (HR-TEM) images of CuCoO$_2$ are illustrated in Figure 7. As a result, we could assume that the crystallinity of CuCoO$_2$ retains a structure mostly constituted of nanocrystals smaller than 15 nm in diameter. HR-TEM d-spacings are likewise consistent with a mixture of rhombohedral and hexagonal CuCoO$_2$ chalcopyrite phases. The results from the FE-SEM agree with the HR-TEM images, which show clearly established small grains of some tens of nanometers.
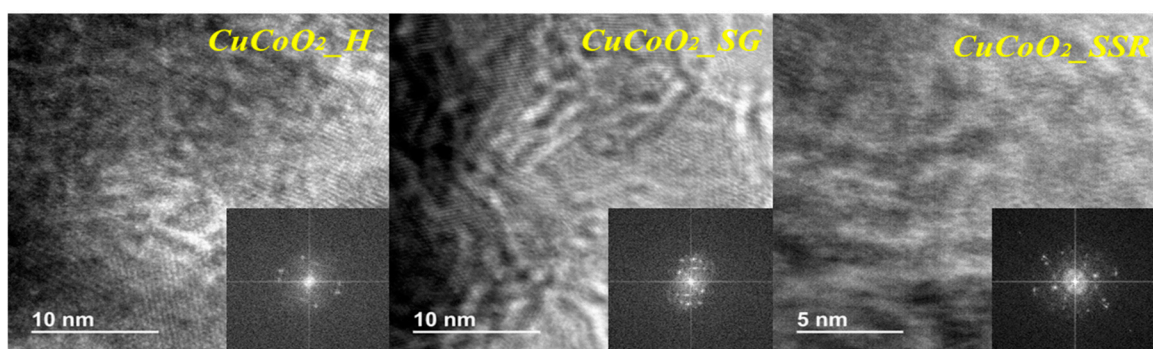

Figure 7. HR-TEM images of CuCoO$_2$_H, CuCoO$_2$_SG, and CuCoO$_2$_SSR.

Figure 8 depicts the transmission electron microscopy (HR-TEM) mapping. The photos of the three CuCoO$_2$ powders reveal a good distribution of copper–cobalt oxide components, with the hydrothermal CuCoO$_2$ powder having a higher crystallinity.
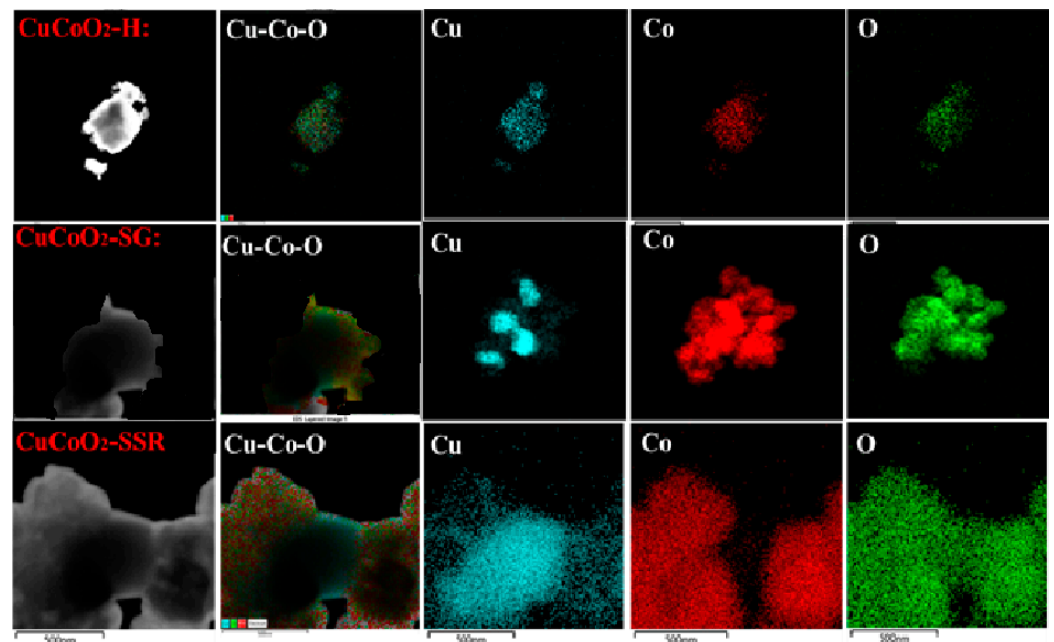
Figure 8. Element mapping analysis of CuCoO$_2$ with TEM.

4. EDX Analysis

We further investigate the chemical composition of our sample using the EDS technique. In Figure 9 and tables below we show the results of the EDS analysis for the cracked surfaces of the CuCoO$_2$_H, CuCoO$_2$_SG, and CuCoO$_2$_SSR samples. From the table above, the percentages of each Cu and Co in a position are approximately the same, but the percent of oxygen is a bit high. This difference may be due to the oxidation of copper or cobalt.

Position	%Atomic		
	Cu	*Co*	*O*
1	23.57	24.68	51.75
2	24.64	24.98	50.38
3	24.57	23.60	51.83
4	26.20	25.65	48.14
Moy	24.75	25.25	50.00

Figure 9. *Cont.*

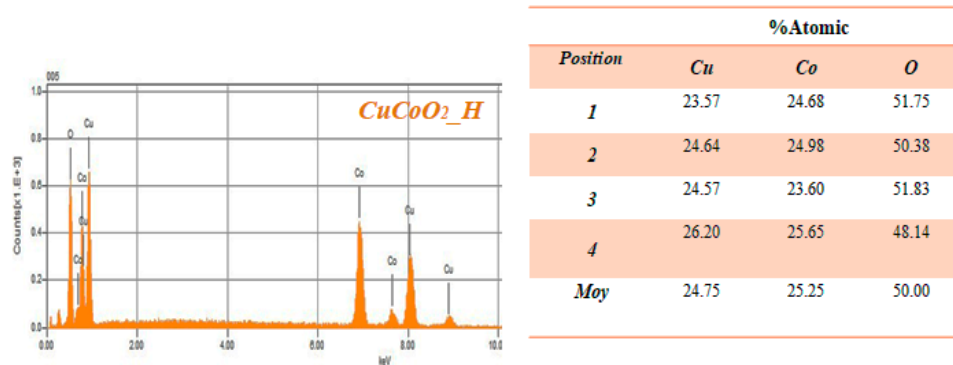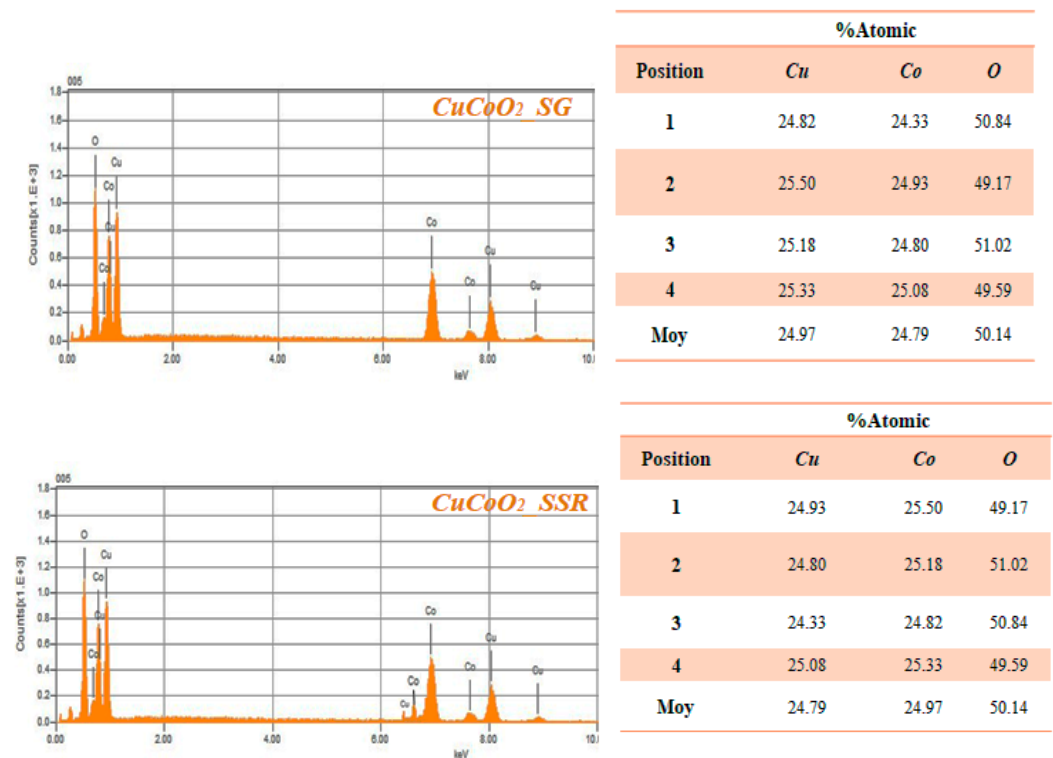| %Atomic			
Position	Cu	Co	O
1	24.82	24.33	50.84
2	25.50	24.93	49.17
3	25.18	24.80	51.02
4	25.33	25.08	49.59
Moy	24.97	24.79	50.14

%Atomic			
Position	Cu	Co	O
1	24.93	25.50	49.17
2	24.80	25.18	51.02
3	24.33	24.82	50.84
4	25.08	25.33	49.59
Moy	24.79	24.97	50.14

Figure 9. Cracked surface test results of three $CuCoO_2$ powders using EDS.

5. Optical Properties

The transmittance spectra have been used to examine optical qualities. In the visible area, all of the $CuCoO_2$ thin films displayed extensive absorption. The absorbance coefficients for thin film samples generated utilizing a spray pyrolysis method containing nanocrystals were determined. In the transmittance spectrum of materials, the absorption coefficient is connected with the optical energy gap or it is in the strong absorption zone, which may be estimated using Tauc's equation [74]

$$\alpha = \frac{A\left(h\nu - E_g\right)^n}{h\nu} \tag{3}$$

A is a constant, *h* is the Planck constant, *ν* is the frequency, and n is an indicator of the optical absorption process. It equals 2 for directly permitted transitions and 0.5 for indirectly permitted transitions. Figure 10 shows (a) the transmission values and (b) the Tauc plot for $CuCoO_2$ thin films. The arrangement of Tauc's figure suggests that the $CuCoO_2$ thin film under deposit has a straight band gap. E_g may be estimated by extrapolating by projecting a horizontal line to the point of zero absorption coefficient ($\alpha = 0$). The band gaps were calculated by graphing $(\alpha h\nu)^2$ vs. energy in eV and extrapolating the linear portion of the spectrum ($h\nu$). According to the transmission graph (Figure 10a), the powder $CuCoO_2\_SG$ has the highest transmission value compared to the two other powders $CuCoO_2\_H$ and $CuCoO_2\_SSR$. The order of the delafossite powders transmission is obviously confirmed with the band gap graphs (Figure 10b).

In the Tauc's plot, the "linear part" is selected by examining the absorption data at higher photon energies, where the absorption is predominantly governed by indirect transitions, with its absorption coefficient being practically constant. In our study, the calculation of band gap values has an error of ±0.10 eV and was obtained by taking the linear part of the curve (between 4 and 4.5 eV), fitting these points to a straight line, and extrapolating this line until it intersects the base line (OX axis). The intersection value (in eV) is the direct band gap according to Tauc's model [74]. In our study, the values obtained for our delafossite material are 3.51 ± 0.10 eV, 3.77 ± 0.12 eV, and 3.87 ± 0.10 eV

for $CuCoO_2$-H, $CuCoO_2$-SSR and $CuCoO_2$-SG, respectively. Depending on the number of points chosen in the range considered, it works as if it were a transparent layer with a certain uncertainty. This suggests that delafossite is likely to be a good transmitter of charge carriers, leading to a higher band gap value of around 3.5 eV.
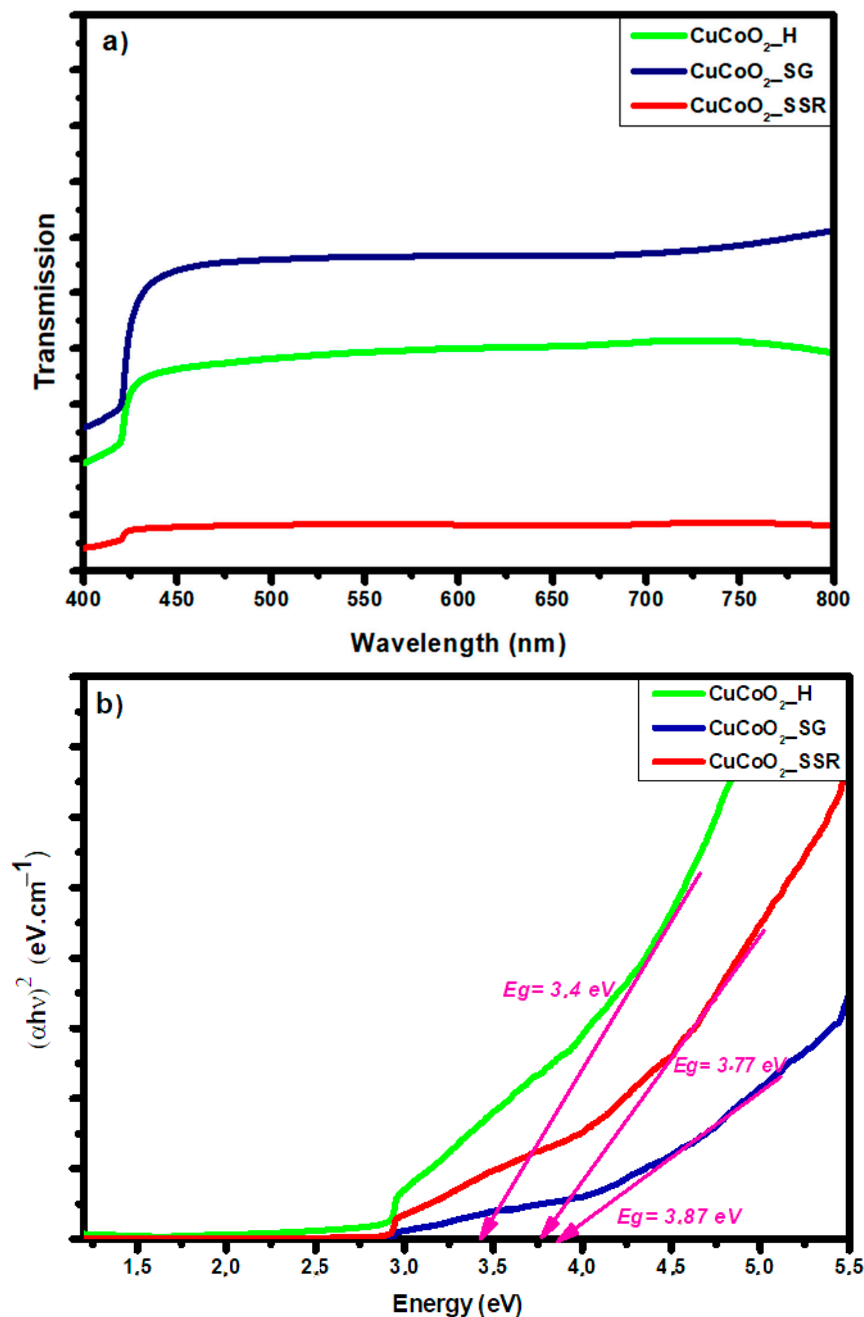

Figure 10. (**a**) Transmission and (**b**) Tauc's plot for $CuCoO_2$_H, $CuCoO_2$_SG, and $CuCoO_2$_SSR precursor powders.

6. In-Plane Conductivity Measurements

In powders used for solar cells, the four-point probe method is the most often used method for assessing the electrical characteristics of conducting films [78,79]. This approach has been utilized to evaluate the in-plane conductivity of $CuCoO_2$ films on top of non-conductive substrates (in our instance, glass), which are typically created by spray pyrolysis technology of the dispersions employed in this work. The experimental procedure used is the following. The four-point probe is attached to a source meter that supplies a certain current. A

source meter's current (I) flows through the two outer probes, and a voltammeter can measure the voltage (V) across the two inner probes. By plotting the voltage measured for each current intensity, the sheet resistance, Rs, can be determined, as is shown in Figure 11.
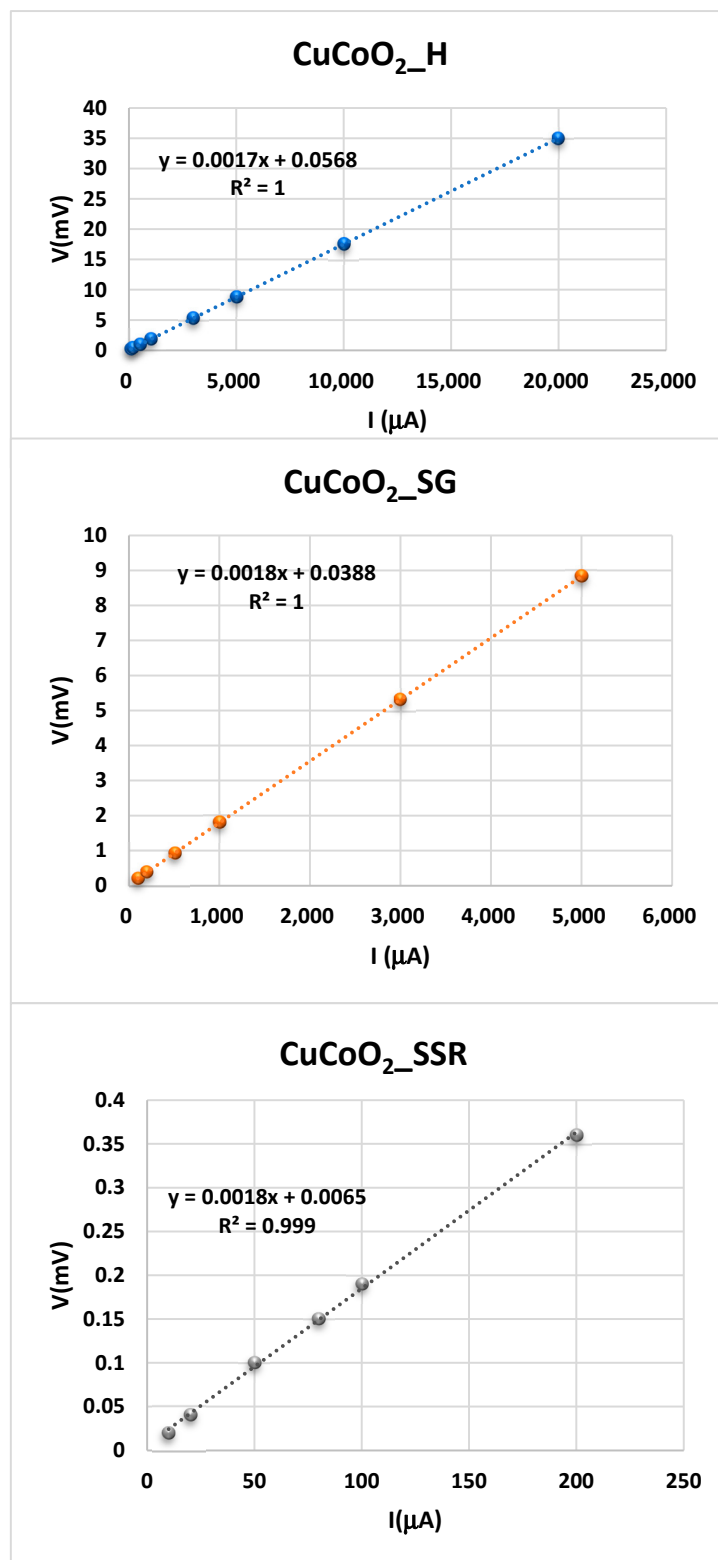

Figure 11. Variation of the potential between RE and S electrodes when a current intensity is given between WE and CE electrodes for the samples $CuCoO_2$ thin films. (●), $CuCoO_2\_H$, (●) $CuCoO_2\_SG$, and (●) $CuCoO_2\_SSR$, at ambient temperature.

A close inspection of these figures reveals that sample resistance (R_s) of the CuCoO$_2$ films is constant, and its values can be obtained from the slope of the experimental fit determined from the plot of the voltage versus intensity, where a clear linearity is observed for all the samples. According to the KIT used to measure the resistance of the film by means of the four-points method, the value of R_s is given by

$$R_s = 4.532 \times \frac{V}{I} \tag{4}$$

The value for said KIT as a consequence of the geometry used in the measurement is the constant 4.532. Therefore, the in-plane conductivity, given in Equation (3), is determined from the sheet resistance from Equation (4). The results of the three produced CuCoO$_2$ samples using the four-point probe technique and measured at ambient temperature are presented in Table 1. The conductivity values change with the chelating agent and the aging duration. These findings imply that aging period and thickness change have an effect on electrical conductivities.

Table 1. The electrical properties of the CuCoO$_2$ thin films determined at ambient temperature.

Samples	Thickness (nm)	Sheet Resistivity (ρ_s) $\times 10^{-3}$ ($\Omega \cdot$cm)	Sheet Resistance (R_s) (Ω)	Sheet Conductivity $\times 10^3$ (S$\cdot$cm^{-1})
CuCoO$_2$_H	140 $\pm$ 5	0.114 $\pm$0.002	8.16 $\pm$ 0.05	8.8 $\pm$ 0.2
CuCoO$_2$_SG	136 $\pm$ 5	0.105 $\pm$ 0.002	7.70 $\pm$ 0.04	9.5 $\pm$ 0.2
CuCoO$_2$_SSR	142 $\pm$ 5	0.116 $\pm$ 0.002	8.16 $\pm$ 0.04	8.6 $\pm$ 0.2

7. Dielectric Spectra Analysis

The electrical impedance spectroscopy (EIS) measurements were performed on all samples to determine the conductivity measured in the transversal direction, named direct current conductivity (σ_{dc}). Such measurements were carried out over a temperature interval of 20 °C to 120 °C in two steps to ensure reproducibility within the temperature interval. The experimental data obtained for the samples from the Novocontrol were examined to obtain the complex dielectric permittivity function, denoted as $\varepsilon^*(\omega,T)$; and the complex conductivity function, denoted as $\sigma^*(\omega,T)$, where j is the imaginary unit ($j^2 = -1$), ε_0 is the vacuum permittivity, and ω is the angular frequency of the electric field that was applied ($\omega = 2\pi f$). Different methods have been used to determine the dc-conductivity of a sample from dielectric spectroscopy data analysis [80–90]. In this work, we have used the Bode diagram obtained from the complex dielectric spectra, where the complex conductivity is given by $\sigma^*(\omega,T) = j\,\varepsilon_0\,\omega\,\varepsilon^*(\omega,T)$, which can be expressed in terms of the real and imaginary part, $\sigma'(\omega,T)$ and $\sigma''(\omega,T)$, respectively, and the direct current conductivity σ_{dc} was calculated [91–94]. This technique was used in this study to examine data for the real component of conductivity in dry conditions by graphing conductivity (in S cm^{-1}) vs. frequency (in Hz) using the appropriate Bode diagrams for all temperature ranges.

The Bode diagrams for CuCoO$_2$_H, CuCoO$_2$_SG, and CuCoO$_2$_SSR delafossite materials were investigated at temperatures ranging from −20 °C to 120 °C, with increments of 20 °C, as shown in Figure 12. Additional graphs demonstrating the variation of phase angle (ϕ) vs. frequency at identical temperatures are included in the Supplementary Materials. Upon closer examination of the figures, it can be observed that the conductivity tends to a constant value (plateau) when the phase angle (ϕ) approaches zero or reaches a maximum, indicating the direct-current conductivity (σ_{dc}) of the sample. Furthermore, a decrease in conductivity with decreasing frequency was observed in the high-frequency region, along with a transition zone where the cut-off frequency ranges from 10^5 to 10^6 Hz for CuCoO$_2$_SG and CuCoO$_2$_SSR samples and starts increasing with frequency. In the case of the hydrothermal sample CuCoO$_2$_H, the real part of conductivity remains constant at low frequencies until a cut-off frequency between 10^3 Hz and 10^6 Hz, after which it starts in-

creasing with frequency. The initial process is connected to the sample's resistance/stability, but this second process is connected to the dispersion (charge transfer) caused by the charge's mobility, as the sample behaves like a capacitor. The conductivity values presented were derived using the peak frequency when the phase angle approaches 0.
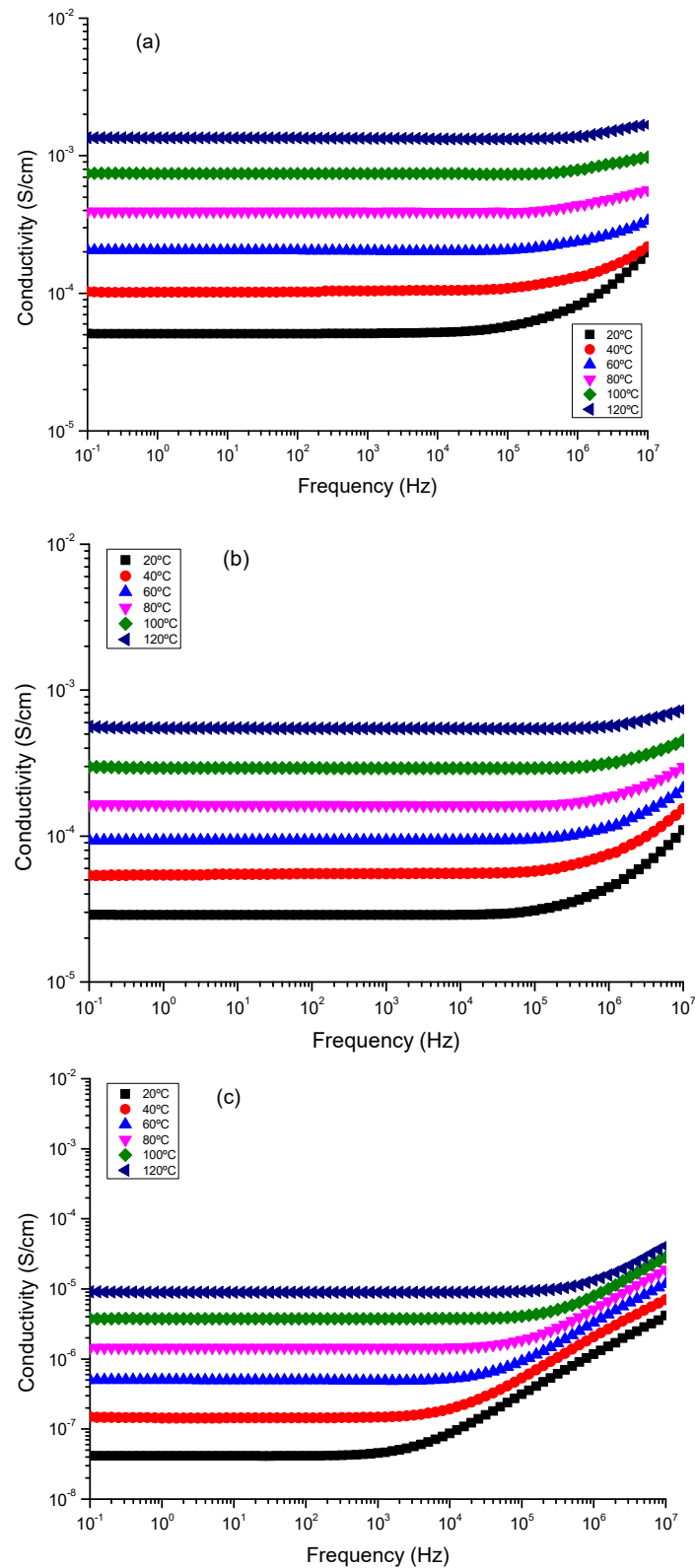

Figure 12. Bode diagrams of the conductivity for (**a**) $CuCoO_2\_SG$, (**b**) $CuCoO_2\_SSR$, and (**c**) $CuCoO_2\_H$ at different temperatures.

Upon careful examination of Figure 12, it can be observed that samples CuCoO$_2$_SG and CuCoO$_2$_SSR exhibit a nearly constant conductivity across a wide range of frequencies and temperatures; that is standard behavior for a conductive material. Identical behavior has been reported in previous studies on nanocomposites of multilayer graphene in polypropylene [95]. This phenomenon is due to Debye relaxation, which occurs as a result of the mobility and redirection of dipoles and localized charges at high frequencies in response to an applied electric field and dominates direct-current conductivity [91,92,96]. The change in dc-conductivity of the samples at various temperatures may be determined from the plateau where the phase angle is zero or tends to zero. For frequencies where the phase is near zero, we have a pure resistive impedance that can be attributed to the ionic conductivity alone. This value is the active phase with high-efficiency electrochemical processes and respects the charge transport into the powders. These phenomena are observed for all the samples at frequencies below 10^4 Hz. Moreover, with rising temperature, the frequency at which the point of equilibrium occurs moves to high frequencies, where a plateau in the Bode diagram from low to high frequencies can be observed, suggesting thermal activation of ionic transport. The constant value of conductivity suggests that the sample solely shows resistive contribution, and the quantity measured represents the sample's electrical conductivity. For example, Figure 12 shows that at 20 °C, the trough plane conductivity values followed the trend: σ_{CuCoO2_SG} (5.2×10^{-5} S cm^{-1}) > σ_{CuCoO2_SSR} (2.9×10^{-5} S cm^{-1}) > σ_{CuCoO2_H} (4.53×10^{-8} S cm^{-1}). Similar trends can be observed for the other temperatures studied (for example, 40 °C, 60 °C, 80 °C, 100 °C and 120 °C). For 120 °C the conductivity values obtained, follow the trend, σ_{CuCoO2_SG} (1.4×10^{-3} S cm^{-1}) > σ_{CuCoO2_SSR} (5.7×10^{-4} S cm^{-1}) > σ_{CuCoO2_H} (1.0×10^{-5} S cm^{-1}), respectively. Among the three samples, the greatest proton conductivity of about 10^{-3} S cm^{-1} at 120 °C was found for the CuCoO$_2$_SG sample and was one order of magnitude higher than CuCoO$_2$_SSR, where excellent ionic conductivities of about 10^{-4} S cm^{-1} were also shown. These results showed that the preparation method used is very relevant to obtaining excellent results in the measured transversal conductivity; in our case, around of one order of magnitude better than sample CuCoO$_2$_H was reached. All these values have better conductivities than CIGS:Cr crystalline nanopowders and CuInGaSe$_2$ (CIGS) chalcopyrite thin films doped with Cr in varying concentrations [93].

From the plot shown in Figure 13, we observe that dc-conductivity increases with the increase of temperature of all mixtures, following an Arrhenius behavior for the thermal activation energy. The measurements of the activation energy calculated from the slopes follow the trend E$_{act}$ (CuCoO$_2$_SSR) = 27.4 kJ/mol < E$_{act}$ (CuCoO$_2$_SG) = 30.8 kJ/mol < E$_{act}$ (CuCoO$_2$_H) = 52.3 kJ/mol, respectively.

These results indicate that the thin films prepared from hydrothermal synthesis have higher activation energy and lower conductivities than the samples prepared from (a) a solid-state reaction where stoichiometric amounts of the above-mentioned powders have been ground with ethanol solution and, after, calcined at a temperature of 800 °C for 5 h. (b) sol-gel; copper(II) nitrate and cobalt(II) nitrate were mixed in ethylene glycol, and after the gelation occurred, it was placed on a magnetic stirring hot plate until a purple color appeared and the substance become darker. The amorphous powder was heated until 800 °C by steps of 50 °C.

Figure 14 shows the relationship between the relaxation time obtained from the cut-off frequency where the conductivity changes from a constant value in the Bode diagram (plateau) to increasing with frequency increase for all temperatures. In such circumstances, such as is observed here in the case of CuCoO$_2$_H (see Figure 12c) for all temperatures, according to the power low model, the real part of the conductivity $\sigma'(\omega,T)$ can be expressed in terms of dc-conductivity σ_{dc} and the hopping diffusion rate of protons $\omega_H \approx 1/\tau$ (in this case) as [94]

$$\sigma'(\omega, T) = \sigma_{dc}\left[1 + \left(\frac{\omega}{\omega_H}\right)^n\right] \tag{5}$$

where n is an exponent with a value between 0 and 1 and is related to interactions between mobile ions (H^+ in our case) and the dimensionally of the conduction pathway [97]; for instance, this occurs in polymer electrolytes of P[VBTC][Cl]$_{80}$-ran-PMMA$_{20}$ at different temperatures (303 K to 363 K) and P[VBTC][TFSIl]$_{80}$-ran-PMMA$_{20}$ at (308 K to 378 K), respectively [98]. From the fit of the real part of the conductivity shown in the Bode diagrams in Figure 12, we have obtained the values of sample relaxation time; these values are plotted in Figure 14 for each temperature.
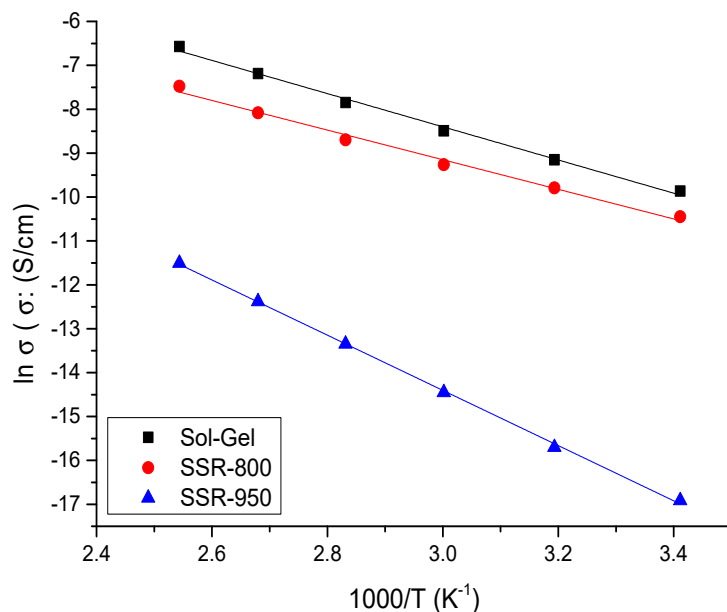

Figure 13. Temperature dependence of conductivity determined using Bode graphs for all samples examined.

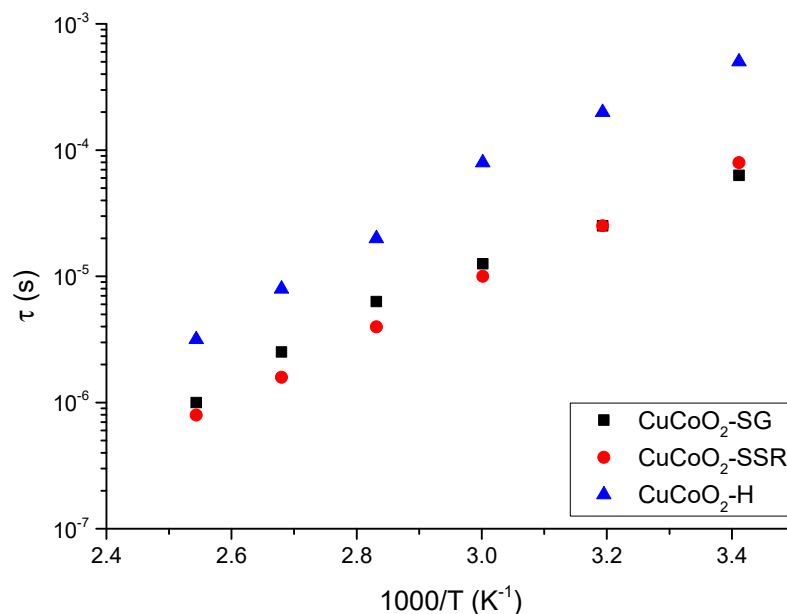

Figure 14. Variation of the sample relaxation time against the reciprocal of temperature for the delafossites investigated.

From Figure 14, we can see that the relaxation time follows an Arrhenius behavior in all the powders studied, but it is interesting to observe that samples prepared using method 2 (CuCoO$_2$_SSR) and method 3 (CuCoO$_2$_SG) have a relaxation time around one order of

magnitude smaller than the sample prepared using he method 1 ($CuCoO_2$_H). This means that the method to produce powders to build thin films is very important to determine their optical and electrical properties. In these results, we observe that delafossites are extremely sensitive to a wide variety of parameters: in particular, the method used in its preparation. The results indicate that these materials have potential in thin film solar cells.

8. Theoretical Insight

Theoretical simulations are critical in the understanding of the properties of systems at the atomic level. Therefore, first-principles calculations were performed to complement the experimental results with an insight on the electronic structure and properties. For this purpose, the atomic positions were optimized, and the electronic properties were computed within the Density Functional Theory (DFT) approach. This was conducted based on the framework of the generalized Kohn–Sham scheme [99–101] in combination with the projector augmented-wave (PAW) method [102] and the Heyd–Scuseria–Ernzerhof hybrid functional with the modified fraction of screened short-range Hartree–Fock exchange (HSE06) [103–105] as implemented in the Vienna ab initio simulation package (VASP) [106–110]. Hybrid functionals allow for a more accurate description of electronic properties of some systems compared to simple DFT calculations with a generalized gradient approximation for the exchange and correlation term in the Kohn–Sham scheme. The higher accuracy, however, is reached at the cost of a higher computational time needed to achieve convergence.

To model the $CuCoO_2$ in the tetragonal phase, a unit cell with 12 atoms ($Co_3Cu_3O_6$) was used, while for the hexagonal cell, a smaller cell with 8 atoms ($Co_2Cu_2O_4$) was needed. The electronic wave functions were expanded in a plane wave basis setup to a kinetic energy cutoff of 400 eV. The atomic positions were optimized using the conjugate gradient method up until the forces on each atom were less than 0.01 eV A^{-1}; and the energy convergence was less than 10^{-8} eV for the optimization and less than 10^{-5} eV for calculations with the hybrid functional. For the Brillouin zone integration, a $12 \times 12 \times 6$ Monkhorst–Pack scheme k-point mesh was used [111–114] both for the optimization and the electronic structure calculation.

Figure 15 shows the atom positions and geometrical structure of the converged unit cells. The delafossite structure of this ternary oxide can be appreciated fairly. In the tetragonal structure, an alternate stacking of O-Cu-O dumbbells lie parallel to the *z* axis, and there is a layer of Co-centered octahedrons in the *xy* plane. The stacking follows an ABCABC pattern, forming a trigonal system with lattice parameters a = 2.86 Å and c = 16.98 Å, corresponding to a rhombohedral Bravais lattice of volume 120.1 Å^3, which matches the experimental data [52,99]. In the hexagonal cells, the same layers of O-Cu-O dumbbells and Co-centered octahedron are observed, but with an ABAB stacking pattern. The lattice constant a = 2.83 Å is practically identical, but c = 11.30 Å is significantly lower; the unit cell volume of 78.47 Å^3 is also lower. However, these differences are due to the fact that a smaller distance is enough to represent the structure because of the stacking sequence. Hence, important distances within the unit cell, such as the distances between O atoms in the O-Cu-O dumbbells (3.71 Å for the tetragonal 3.69 Å in the hexagonal) or the distances from a cornered O to a centered Co in the octahedron (1.92 Å for the tetragonal and 1.91 Å in the hexagonal) are practically the same.

The band structure and density of states for the tetragonal phase can be appreciated in Figure 16. Though the inclusion of the hybrid functional allows the possibility of avoiding the typical underestimation of gaps in pure DFT approaches; the bandgap values obtained seems to remain underestimated: 2.31 eV for the tetragonal structure and 2.34 for the hexagonal one (experimental results are between 2.5 to 3.65 eV [77,98,103]). However, the structure of the bands and the form of the density of states of the curves are usually well described in this type of calculations, and despite the small difference in bandgap values for both structures, the form of the density of states is practically the same, so only one of them is plotted.
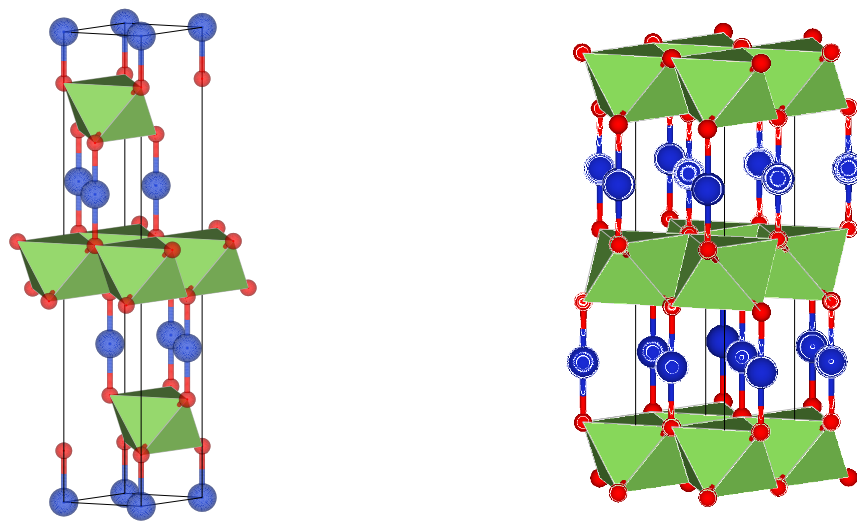
Figure 15. Trigonal and hexagonal structures of CuCoO$_2$. The atoms of Cu are represented in blue; O atoms are presented in red; and the metal atoms lie inside the green octahedron.
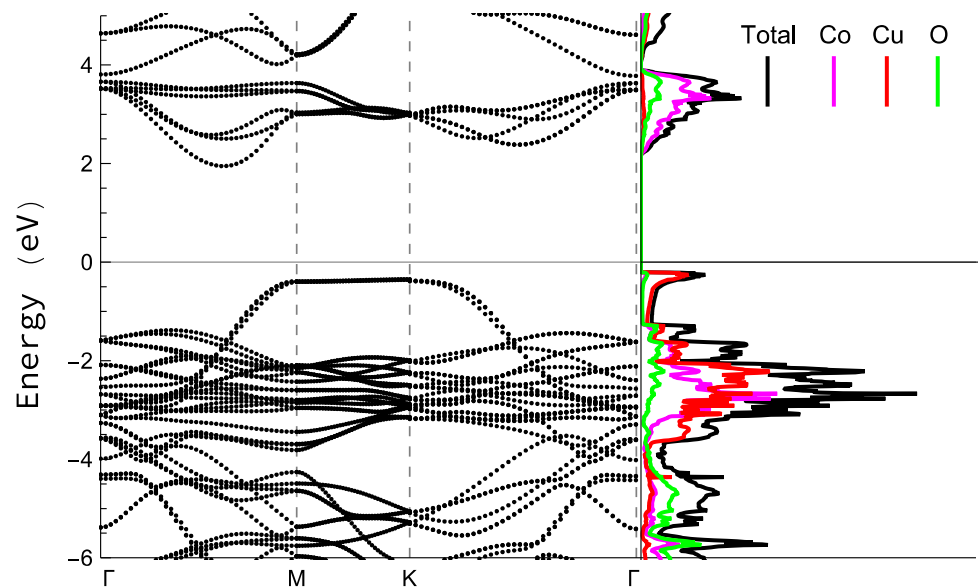

Figure 16. Bands structure (**left**) and states' density (**right**) acquired by HSE simulations for the tetragonal structure. Energies are expressed with respect to the Fermi energy. Black line accounts for total DOS in the right part, and colored lines accounts for the contribution of every species to the density of states: Co atoms are represented by pink, Cu atoms by red, and O atoms by green.

The obtained gap is an indirect one, which can be appreciated by simple inspection of the bands structure in the left part of Figure 16. The right part shows the density of states in which it is appreciable that the edge of the covalent band is apparently dominated by Cu-3d states. O states show a wide dispersion through the band, but the presence of Co-3d states is high in this region and, except for the peak at the edge of the band, is comparable with the contribution from Cu states. Also, the first peak in the conduction band is mainly due to Co-3d states followed by a second peak with a structure similar to the one that can be found in CuAlO$_2$. and CuGaO$_2$, as it has been previously reported [98,99,103].

9. Conclusions

In summary, the preparation of delafossite CuCoO$_2$ using three cost-effective techniques yields a well-ordered crystalline mixture comprising two structures: rhombohedral and hexagonal, exhibiting similar properties and favorable band gap values. To ensure the

development of an effective coating solution, careful treatment of the resultant nano-sized precursor powder is necessary. The desired thin films, namely $CuCoO_2\_H$ (produced via hydrothermal method), $CuCoO_2\_SG$ (produced via sol-gel method), and $CuCoO_2\_SSR$ (produced via solid-state reaction method), were successfully obtained through the spray pyrolysis process. Electrochemical impedance spectroscopy measurements reveal that the Sol-Gel method yields films with superior conductivity compared to the other preparation methods. As a result, $CuCoO_2$ thin films hold significant potential for solar cell applications. This is supported by the examination of the electronic properties of the rhombohedral $CuCoO_2$ through theoretical simulations. Furthermore, electrochemical impedance spectroscopy measurements demonstrate that the copper cobalt delafossites prepared using different synthesis methods have the potential to serve as semiconductor materials. The conductivity values, measured through the plane, increase with temperature as expected: $\sigma_{cucoo2\_sg} > \sigma_{cucoo2\_ssr} > \sigma_{cucoo2\_h}$. Among the three samples, $CuCoO_2\_SG$ exhibits the highest conductivity of approximately 10^{-3} S cm^{-1} at 120 °C, which is one order of magnitude greater than $CuCoO_2\_SSR$, while still maintaining good ionic conductivities of approximately 10^{-4} S cm^{-1}. This value is approximately two orders of magnitude higher than that of $CuCoO_2\_H$. These conductivity measurements, obtained through impedance spectroscopy, are in agreement with the values determined using the four-probe method, where resistivity follows the trend of $\rho_{CuCoO2\_SG} < \rho_{CuCoO2\_SSR} \approx \rho_{CuCoO2\_H}$. Lastly, our study demonstrates that samples prepared using method 2 ($CuCoO_2\_SSR$) and method 3 ($CuCoO_2\_SG$) have relaxation times approximately one order of magnitude smaller than samples prepared using method 1 ($CuCoO_2\_H$). This result emphasizes the significant impact that the synthesis method and sample preparation can have on producing powders for building thin films to enhance optical and electrical properties, particularly for solar cell applications.

Supplementary Materials: The following supporting information can be downloaded at: https://www.mdpi.com/article/10.3390/nano13162312/s1, Figure S1: Phase angle (φ) corresponding to the Bode diagrams for (a) $CuCoO_2\_H$, (b) $CuCoO_2\_SG$, and (c) $CuCoO_2\_SSR$ delafossite materials at temperatures ranging from −20 °C to 120 °C, with increments of 20 °C, as shown.

Author Contributions: Conceptualization, H.C., J.C.T. and V.C.; methodology, J.C.T., A.B., B.M.S. and V.C.; software, H.C. and A.A.; validation, A.B., M.A.L. and V.C.; formal analysis, H.C., A.B., A.A., P.P. and V.C.; investigation, A.B., A.A., B.M.S., P.P., M.A.L. and V.C.; data curation, H.C. and A.A.; writing—original draft preparation, A.A., B.M.S., P.P. and V.C. writing—review and editing, A.B. and V.C.; supervision, A.B. and V.C.; project administration, B.M.S. and V.C.; funding acquisition, B.M.S.; All authors have read and agreed to the published version of the manuscript.

Data Availability Statement: The data presented in this study are available on request from the corresponding author.

Conflicts of Interest: The authors declare no conflict of interest.

References

1. Ai, B.; Fan, Z.; Wong, Z.J. Plasmonic–perovskite solar cells, light emitters, and sensors. *Microsyst. Nanoeng.* **2022**, *8*, 5. [CrossRef]
2. Fukuda, K.; Yu, K.; Someya, T. The Future of Flexible Organic Solar Cells. *Adv. Energy Mater.* **2020**, *10*, 2000765. [CrossRef]
3. Sehrawat, P.; Malik, R.K.; Khatkar, S.P.; Taxak, V.B. Highly efficient green-glimmering $Y_3Al_5O_{12}$: Er^{3+} NPs for next generation electro-optic appliances, mainly white-LEDs and solar-cells. *Chem. Phys. Lett.* **2021**, *773*, 138592. [CrossRef]
4. Sargent, E.H. Solar Cells, Photodetectors, and Optical Sources from Infrared Colloidal Quantum Dots. *Adv. Mater.* **2008**, *20*, 3958–3964. [CrossRef]
5. Cappelli, I.; Carli, F.; Fort, A.; Micheletti, F.; Vignoli, V.; Bruzzi, M. Self-Sufficient Sensor Node Embedding 2D Visible Light Positioning through a Solar Cell Module. *Sensors* **2022**, *22*, 5869. [CrossRef] [PubMed]

6.   Dinh, N.N.; Khanh, T.S.T.; Long, L.M.; Cuong, N.D.; Nam, N.P.H. Nanomaterials for Organic Optoelectronic Devices: Organic Light-Emitting Diodes, Organics Solar Cells and Organic Gas Sensors. *Mater. Trans.* **2020**, *61*, 1422–1429. [CrossRef]

7.   Dai, B.; Biesold, G.M.; Zhang, M.; Zou, H.; Ding, Y.; Wang, Z.L.; Lin, Z. Piezo-phototronic effect on photocatalysis, solar cells, photodetectors and light-emitting diodes. *Chem. Soc. Rev.* **2021**, *50*, 13646–13691. [CrossRef]

8.   Xu, J.; Shalom, M. Conjugated Carbon Nitride as an Emerging Luminescent Material: Quantum Dots, Thin Films and Their Applications in Imaging, Sensing, Optoelectronic Devices and Photoelectrochemistry. *Chemphotochem* **2019**, *3*, 170–179. [CrossRef]

9.   Youn, D.H.; Choi, Y.H.; Kim, J.H.; Han, S.; Heller, A.; Mullins, C.B. Simple Microwave-Assisted Synthesis of Delafossite $CuFeO_2$ as an Anode Material for Sodium-Ion Batteries. *ChemElectroChem* **2018**, *5*, 2419–2423. [CrossRef]

10.   Amrute, A.P.; Łodziana, Z.; Mondelli, C.; Krumeich, F.; Perez-Ramirez, J. Solid-state chemistry of cuprous delafossites: Synthesis and stability aspects. *Chem. Mater.* **2013**, *25*, 4423–4435. [CrossRef]

11.   Sheets, W.C.; Mugnier, E.; Barnabé, A.; Marks, T.J.; Poeppelmeier, K.R. Hydrothermal Synthesis of Delafossite-Type Oxides. *Chem. Mater.* **2006**, *18*, 7–20. [CrossRef]

12.   Karati, A.; Parida, T.; Gupta, J.; Adigilli, H.K.; Borse, P.H.; Joardar, J. Band-gap engineering in novel delafossite-type multicomponent oxides for photocatalytic degradation of methylene blue. *Mater. Res. Bull.* **2021**, *137*, 111181. [CrossRef]

13.   Singh, A.N.; Mondal, R.; Rath, C.; Singh, P. Electrochemical Performance of Delafossite, $AgFeO_2$: A Pseudo-Capacitive Electrode in Neutral Aqueous Na_2SO_4 Electrolyte. *J. Electrochem. Soc.* **2021**, *168*, 120512. [CrossRef]

14.   Bennett, J.W.; Jones, D.T.; Hudson, B.G.; Melendez-Rivera, J.; Hamers, R.J.; Mason, S.E. Emerging investigator series: First-principles and thermodynamics comparison of compositionally-tuned delafossites: Cation release from the (001) surface of complex metal oxides. *Environ. Sci. Nano* **2020**, *7*, 1642–1651. [CrossRef]

15.   Dong, Y.; Cao, C.; Chui, Y.-S.; Zapien, J.A. Facile hydrothermal synthesis of $CuFeO_2$ hexagonal platelets/rings and graphene composites as anode materials for lithium ion batteries. *Chem. Commun.* **2014**, *50*, 10151–10154. [CrossRef] [PubMed]

16.   Liu, Y.; Gong, Y.; Mellott, N.P.; Wang, B.; Ye, H.; Wu, Y. Luminescence of delafossite-type $CuAlO_2$ fibers with Eu substitution for Al cations. *Sci. Technol. Adv. Mater.* **2016**, *17*, 200–209. [CrossRef]

17.   Fujishiro, F.; Murakami, M.; Hashimoto, T.; Takahashi, M. Orange luminescence of Eu^{3+}-doped $CuLaO_2$ delafossite oxide. *J. Ceram. Soc. Jpn.* **2010**, *118*, 1217–1220. [CrossRef]

18.   Jacob, A.; Parent, C.; Boutinaud, P.; Le Flem, G.; Doumerc, J.; Ammar, A.; Elazhari, M.; Elaatmani, M. Luminescent properties of delafossite-type oxides $LaCuO_2$ and $YCuO_2$. *Solid State Commun.* **1997**, *103*, 529–532. [CrossRef]

19.   Zhao, T.; Liu, Q.L.; Zhao, Z.Y. High-throughput screening delafossite $CuMO_2$ (M = IIIA, 3d, 4d, 5d, and RE) optoelectronic functional materials based on first-principles calculations. *J. Phys. Chem. C* **2019**, *123*, 14292–14302. [CrossRef]

20.   Tsuboi, N.; Ohara, H.; Hoshino, T.; Kobayashi, S.; Kato, K.; Kaneko, F. Luminescence properties of delafossite-type $CuYO_2$ doped with calcium, oxygen or rare earth Tb. *Jpn. J. Appl. Phys.* **2005**, *44*, 765. [CrossRef]

21.   Siedliska, K.; Pikula, T.; Oleszak, D.; Jartych, E. Structure and Hyperfine Interactions of Mechanically Activated Delafossite $CuFeO_2$. *Acta Phys. Pol. A* **2018**, *133*, 372–375. [CrossRef]

22.   Daou, R.; Frésard, R.; Eyert, V.; Hébert, S.; Maignan, A. Unconventional aspects of electronic transport in delafossite oxides. *Sci. Technol. Adv. Mater.* **2017**, *18*, 919–938. [CrossRef] [PubMed]

23.   Okuda, T.; Jufuku, N.; Hidaka, S.; Terada, N. Magnetic, transport, and thermoelectric properties of the delafossite oxides $CuCr_{1-x}Mg_xO_2$ ($0 \leq x \leq 0.04$). *Phys. Rev. B* **2005**, *72*, 144403. [CrossRef]

24.   Van Hoang, D.; Pham, A.T.T.; Ta, H.K.T.; Nguyen, T.H.; Pham, N.K.; Hoa, L.T.; Tran, V.C.; Michitaka, O.; Tran, Q.M.N.; Park, J.-H.; et al. Effects of multi-scale defects on the thermoelectric properties of delafossite $CuCr_{1-x}Mg_xO_2$ materials. *J. Alloys Compd.* **2020**, *844*, 156119. [CrossRef]

25.   Feng, Y.; Elquist, A.; Zhang, Y.; Gao, K.; Ferguson, I.; Tzempelikos, A.; Lu, N. Temperature dependent thermoelectric properties of cuprous delafossite oxides. *Compos. Part B Eng.* **2019**, *156*, 108–112. [CrossRef]

26.   Van Hoang, D.; Le, T.A.K.; Pham, A.T.T.; Ta, H.K.T.; Pham, N.K.; Nguyen, T.H.; Lai, H.T.; Truong, D.C.; Van Le, N.; Huynh, C.T.; et al. The roles of interstitial oxygen and phase compositions on the thermoelectric properties $CuCr_{0.85}Mg_{0.15}O_2$ delafossite material. *J. Alloys Compd.* **2021**, *867*, 158995. [CrossRef]

27.   Ruttanapun, C.; Wichainchai, A.; Prachamon, W.; Yangthaisong, A.; Charoenphakdee, A.; Seetawan, T. Thermoelectric properties of $Cu_{1-x}Pt_xFeO_2$ ($0.0 \leq x \leq 0.05$) delafossite-type transition oxide. *J. Alloys Compd.* **2011**, *509*, 4588–4594. [CrossRef]

28.   Sinnarasa, I.; Thimont, Y.; Presmanes, L.; Bonningue, C.; Barnabé, A.; Tailhades, P. Influence of thickness and microstructure on thermoelectric properties of Mg-doped $CuCrO_2$ delafossite thin films deposited by RF-magnetron sputtering. *Appl. Surf. Sci.* **2018**, *455*, 244–250. [CrossRef]

29.   Liu, Q.-L.; Zhao, Z.-Y.; Zhao, R.-D.; Yi, J.-H. Fundamental properties of delafossite $CuFeO_2$ as photocatalyst for solar energy conversion. *J. Alloys Compd.* **2018**, *819*, 153032. [CrossRef]

30.   Liu, Q.L.; Zhao, Z.Y.; Yi, J.H. Excess oxygen in delafossite $CuFeO_2+ \delta$: Synthesis, characterization, and applications in solar energy conversion. *Chem. Eng. J.* **2020**, *396*, 125290. [CrossRef]

31.   Dong, X.-D.; Zhao, Z.-Y. Boosting and regulating solar energy conversion performance of delafossite $AgFeO_2$ by spin polarization. *J. Mater. Chem. A* **2022**, *10*, 4800–4816. [CrossRef]

32.   Zhao, R.-D.; Zhang, Y.-M.; Liu, Q.-L.; Zhao, Z.-Y. Effects of the Preparation Process on the Photocatalytic Performance of Delafossite $CuCrO_2$. *Inorg. Chem.* **2020**, *59*, 16679–16689. [CrossRef] [PubMed]

33. Zhao, Q.M.; Zhao, Z.Y.; Liu, Q.L.; Yao, G.Y.; Dong, X.D. Delafossite CuGaO$_2$ as promising visible-light-driven photocatalyst: Synthesize, properties, and performances. *J. Phys. D Appl. Phys.* **2020**, *53*, 135102. [CrossRef]

34. Ahmed, J.; Mao, Y. Synthesis, characterization and electrocatalytic properties of delafossite CuGaO$_2$. *J. Solid State Chem.* **2016**, *242*, 77–85. [CrossRef]

35. Xu, Q.; Li, R.; Wang, C.; Yuan, D. Visible-light photocatalytic reduction of Cr (VI) using nano-sized delafossite (CuFeO$_2$) synthesized by hydrothermal method. *J. Alloys Compd.* **2017**, *723*, 441–447. [CrossRef]

36. Díaz-García, A.K.; Lana-Villarreal, T.; Gómez, R. Sol–gel copper chromium delafossite thin films as stable oxide photocathodes for water splitting. *J. Mater. Chem. A* **2015**, *3*, 19683–19687. [CrossRef]

37. Jang, Y.J.; Lee, J.S. Photoelectrochemical Water Splitting with p-Type Metal Oxide Semiconductor Photocathodes. *Chemsuschem* **2019**, *12*, 1835–1845. [CrossRef] [PubMed]

38. Jang, Y.J.; Bin Park, Y.; Kim, H.E.; Choi, Y.H.; Choi, S.H.; Lee, J.S. Oxygen-Intercalated CuFeO$_2$ Photocathode Fabricated by Hybrid Microwave Annealing for Efficient Solar Hydrogen Production. *Chem. Mater.* **2016**, *28*, 6054–6061. [CrossRef]

39. Prévot, M.S.; Li, Y.; Guijarro, N.; Sivula, K. Improving charge collection with delafossite photocathodes: A host–guest CuAlO$_2$/CuFeO$_2$ approach. *J. Mater. Chem. A* **2016**, *4*, 3018–3026. [CrossRef]

40. Li, C.; He, J.; Xiao, Y.; Li, Y.; Delaunay, J.J. Earth-abundant Cu-based metal oxide photocathodes for photoelectrochemical water splitting. *Energy Environ. Sci.* **2020**, *13*, 3269–3306. [CrossRef]

41. Garcia-Torregrosa, I.; Geertzema, Y.G.; Ismail, A.S.M.; Lee, T.; Groot, F.M.F.; Weckhuysen, B.M. Facile Two-Step Synthesis of Delafossite CuFeO$_2$ Photocathodes by Ultrasonic Spray Pyrolysis and Hybrid Microwave Annealing. *Chemphotochem* **2019**, *3*, 1238–1245. [CrossRef]

42. Deng, Z.; Meng, G.; Fang, X.; Dong, W.; Shao, J.; Wang, S.; Tong, B. A novel ammonia gas sensors based on p-type delafossite AgAlO$_2$. *J. Alloys Compd.* **2019**, *777*, 52–58. [CrossRef]

43. Tong, B.; Deng, Z.; Xu, B.; Meng, G.; Shao, J.; Liu, H.; Dai, T.; Shan, X.; Dong, W.; Wang, S.; et al. Oxygen Vacancy Defects Boosted High Performance p-Type Delafossite CuCrO$_2$ Gas Sensors. *ACS Appl. Mater. Interfaces* **2018**, *10*, 34727–34734. [CrossRef] [PubMed]

44. Upadhyay, D.; Roondhe, B.; Pratap, A.; Jha, P.K. Two-dimensional delafossite cobalt oxyhydroxide as a toxic gas sensor. *Appl. Surf. Sci.* **2019**, *476*, 198–204. [CrossRef]

45. Liu, H.; Cao, X.; Wu, H.; Li, B.; Li, Y.; Zhu, W.; Yang, Z.; Huang, Y. Innovative development on a p-type delafossite CuCrO$_2$ nanoparticles based triethylamine sensor. *Sens. Actuators B Chem.* **2020**, *324*, 128743. [CrossRef]

46. Patzsch, J.; Balog, I.; Krauß, P.; Lehmann, C.W.; Schneider, J.J. Synthesis, characterization and p–n type gas sensing behaviour of CuFeO$_2$ delafossite type inorganic wires using Fe and Cu complexes as single source molecular precursors. *RSC Adv.* **2014**, *4*, 15348–15355. [CrossRef]

47. Beatriceveena, T.; Murthy, A.S.R.; Prabhu, E.; Gnanasekar, K. Wide range hydrogen sensing behavior of a silver delafossite: Performance towards long term stability, repeatability and selectivity. *Int. J. Hydrog. Energy* **2021**, *46*, 2824–2834. [CrossRef]

48. Kong, L.; Xu, S.; Liu, H.; Wu, X.; Tu, X.; Bo, M.; Zhu, W. Hybridized Ag-CuCrO$_2$ Nanostructured Composites for Enhanced Gas Sensing. *ACS Appl. Nano Mater.* **2022**, *5*, 12690–12698. [CrossRef]

49. Liu, H.; Zhao, T.; Kong, L.; Cao, X.; Zhu, W.; Huang, Y.; Bo, M. Twinning enhanced electrical conductivity and surface activity of nanostructured CuCrO$_2$ gas sensor. *Sens. Actuators B Chem.* **2021**, *338*, 129845. [CrossRef]

50. Du, Z.; Xiong, D.; Verma, S.K.; Liu, B.; Zhao, X.; Liu, L.; Li, H. A low temperature hydrothermal synthesis of delafossite CuCoO$_2$ as an efficient electrocatalyst for the oxygen evolution reaction in alkaline solutions. *Inorg. Chem. Front.* **2018**, *5*, 183–188. [CrossRef]

51. Kurita, K.; Yagisawa, M.; Okazaki, R. Electrical resistivity and thermopower of hole-doped delafossite CuCoO$_2$ polycrystals. *Jpn. J. Appl. Phys.* **2021**, *60*, 013001. [CrossRef]

52. Bouakaz, H.; Abbas, M.; Brahimi, R.; Trari, M. Physical properties of the delafossite CuCoO$_2$ synthesized by co-precipitation/hydrothermal route. *Mater. Sci. Semicond. Process.* **2021**, *136*, 106132. [CrossRef]

53. Zhang, Y.M.; Zhao, Z.Y.; Zhao, Y.K.; Wang, C.X. One-pot synthesis of delafossite CuCoO$_2$ microcrystal as visible-light-driven photocatalyst. *J. Mater. Sci.* **2022**, *57*, 18687–18710. [CrossRef]

54. Xiong, D.; Du, Z.; Li, H.; Xu, J.; Li, J.; Zhao, X.; Liu, L. Polyvinylpyrrolidone-Assisted Hydrothermal Synthesis of CuCoO$_2$ Nanoplates with Enhanced Oxygen Evolution Reaction Performance. *ACS Sustain. Chem. Eng.* **2018**, *7*, 1493–1501. [CrossRef]

55. Gao, H.; Yang, M.; Du, Z.; Liu, X.; Dai, X.; Lin, K.; Bao, X.-Q.; Li, H.; Xiong, D. Metal–organic framework derived bimetal oxide CuCoO$_2$ as efficient electrocatalyst for the oxygen evolution reaction. *Dalton Trans.* **2022**, *51*, 5997–6006. [CrossRef]

56. Gao, H.; Liu, X.; Han, N.; Shi, L.; Wang, L.; Mi, Y.; Bao, X.-Q.; Bai, J.; Li, H.; Xiong, D. Nanocrystals of CuCoO$_2$ derived from MOFs and their catalytic performance for the oxygen evolution reaction. *Dalton Trans.* **2022**, *51*, 11536–11546. [CrossRef] [PubMed]

57. Du, Z.; Qian, J.; Bai, J.; Li, H.; Wang, M.; Zhao, X.; Xiong, D. Surfactant-Modified Hydrothermal Synthesis of Ca-Doped CuCoO$_2$ Nanosheets with Abundant Active Sites for Enhanced Electrocatalytic Oxygen Evolution. *Inorg. Chem.* **2020**, *59*, 9889–9899. [CrossRef]

58. Yang, M.; Han, N.; Shi, L.; Gao, H.; Liu, X.; Mi, Y.; Zeng, X.; Bai, J.; Xiong, D. Effect of nickel doping on the structure, morphology and oxygen evolution reaction performance of Cu-BTC derived CuCoO$_2$. *Dalton Trans.* **2022**, *51*, 8757–8765. [CrossRef]

59. Beekman, M.; Salvador, J.; Shi, X.; Nolas, G.; Yang, J. Characterization of delafossite-type CuCoO$_2$ prepared by ion exchange. *J. Alloys Compd.* **2010**, *489*, 336–338. [CrossRef]

60. Toyoda, K.; Hinogami, R.; Miyata, N.; Aizawa, M. Calculated Descriptors of Catalytic Activity for Water Electrolysis Anode: Application to Delafossite Oxides. *J. Phys. Chem. C* **2015**, *119*, 6495–6501. [CrossRef]

61. Miyata, N.; Toyoda, K.; Hinogami, R.; Katayama, M.; Inada, Y.; Ohta, T. Spin states investigation of delafossite oxides by means of X-ray absorption and photoemission spectroscopy. *J. Solid State Chem.* **2019**, *275*, 83–87. [CrossRef]

62. Upadhyay, D.K. Investigation of Structural, Electronic, Magnetic and Dynamical Properties of Transition Metal Doped Delafossite-Type Oxides. Ph.D. Thesis, Maharaja Sayajirao University of Baroda, Baroda, India, 2021.

63. Burlet, C.; Goethals, H.; Vanbrabant, Y. Delafossite structure of heterogenite polytypes ($HCoO_2$) by Raman and infrared micro-spectroscopy. *Spectrochim. Acta Part A Mol. Biomol. Spectrosc.* **2016**, *159*, 90–97. [CrossRef]

64. Du, Z.; Xiong, D.; Qian, J.; Zhang, T.; Bai, J.; Fang, D.; Li, H. Investigation of the structural, optical and electrical properties of Ca^{2+} doped $CuCoO_2$ nanosheets. *Dalton Trans.* **2019**, *48*, 13753–13759. [CrossRef] [PubMed]

65. Isacfranklin, M.; Yuvakkumar, R.; Ravi, G.; Pannipara, M.; Al-Sehemi, A.G.; Velauthapillai, D. $CuCoO_2$ electrodes for supercapacitor applications. *Mater. Lett.* **2021**, *296*, 129930. [CrossRef]

66. Feng, Y.; Liao, J.; Chen, X.; Liao, Q.; Wang, H.; Ji, S.; Pollet, B.G.; Li, H.; He, M. Co_3O_4–$CuCoO_2$ hybrid nanoplates as a low-cost and highly active catalyst for producing hydrogen from ammonia borane. *New J. Chem.* **2021**, *45*, 2688–2695. [CrossRef]

67. Du, Z.; Qian, J.; Zhang, T.; Ji, C.; Wu, J.; Li, H.; Xiong, D. Solvothermal synthesis of $CuCoO_2$ nanoplates using zeolitic imidazolate framework-67 (ZIF-67) as a co-derived precursor. *New J. Chem.* **2019**, *43*, 15233–15239. [CrossRef]

68. Ding, J.; Li, L.; Zheng, H.; Zuo, Y.; Wang, X.; Li, H.; Chen, S.; Zhang, D.; Xu, X.; Li, G. Co_3O_4–$CuCoO_2$ nanomesh: An interface-enhanced substrate that simultaneously promotes CO adsorption and O_2 activation in H_2 purification. *ACS Appl. Mater. Interfaces* **2019**, *11*, 6042–6053. [CrossRef]

69. Zhong, X.; He, H.; Du, J.; Ren, Q.; Huang, J.; Tang, Y.; Wang, J.; Yang, L.; Dong, F.; Bian, L.; et al. Boosting solar water oxidation activity and stability of $BiVO_4$ photoanode through the Co-catalytic effect of $CuCoO_2$. *Electrochim. Acta* **2019**, *304*, 301–311. [CrossRef]

70. Dursun, S.; Akyıldız, H.; Kalem, V. Production of $CuCoO_2$ nanoparticle/SnO_2 nanofiber heterostructures for visible light photocatalytic applications. *J. Photochem. Photobiol. A Chem.* **2023**, *434*, 114233. [CrossRef]

71. Xing, W.; Kong, L.; Zhang, X.; Zhang, Y.; Tu, X.; Yu, J.; Yang, J.; Zhou, C.; Zhu, W.; Huang, J. Enhanced Methanol Electrooxidation Performance Based on Pt Cluster-Decorated $CuCoO_2$ on Carbon. *ChemistrySelect* **2022**, *7*, e202200513. [CrossRef]

72. Mariappan, K.; Chen, S.-M.; Chen, T.-W.; Tseng, T.-W.; Bian, Y.; Sun, T.-T.; Jiang, J.; Yu, J. Fabrication of Hexagonal $CuCoO_2$ Modified Screen-Printed Carbon Electrode for the Selective Electrochemical Detection of Furaltadone. *Int. J. Electrochem. Sci.* **2022**, *17*, 220644. [CrossRef]

73. Ruttanapun, C.; Sa-Nguan-Cheep, M.; Kahatta, S.; Buranasiri, P.; Jindajitawat, P. Optical and electronic transport properties of p-type $CuCoO_2$ transparent conductive oxide. In Proceedings of the ICPS 2013: International Conference on Photonics Solutions, Pattaya City, Thailand, 26–28 May 2013; SPIE: Bellingham, DC, USA, 2013; Volume 8883, pp. 319–325.

74. Makuła, P.; Pacia, M.; Macyk, W. How To Correctly Determine the Band Gap Energy of Modified Semiconductor Photocatalysts Based on UV–Vis Spectra. *J. Phys. Chem. Lett.* **2018**, *9*, 6814–6817. [CrossRef]

75. Müller, F.; Ferreira, C.A.; Franco, L.; Puiggalí, J.; Alemán, C.; Armelin, E. New Sulfonated Polystyrene and Styrene–Ethylene/Butylene–Styrene Block Copolymers for Applications in Electrodialysis. *J. Phys. Chem. B* **2012**, *116*, 11767–11779. [CrossRef] [PubMed]

76. Soboleva, T.; Xie, Z.; Shi, Z.; Tsang, E.; Navessin, T.; Holdcroft, S. Investigation of the through-plane impedance technique for evaluation of anisotropy of proton conducting polymer membranes. *J. Electroanal. Chem.* **2008**, *622*, 145–152. [CrossRef]

77. Blachot, J.F.; Diat, O.; Putaux, J.-L.; Rollet, A.-L.; Rubatat, L.; Vallois, C.; Müller, M.; Gebel, G. Anisotropy of structure and transport properties in sulfonated polyimide membranes. *J. Membr. Sci.* **2003**, *214*, 31–42. [CrossRef]

78. Zawodzinski, T.A.; Derouin, C.; Radzinski, S.; Sherman, R.J.; Smith, V.T.; Springer, T.E.; Gottesfeld, S. Water Uptake by and Transport Through Nafion® 117 Membranes. *J. Electrochem. Soc.* **1993**, *140*, 1041–1047. [CrossRef]

79. Escorihuela, J.; Narducci, R.; Compañ, V.; Costantino, F. Proton Conductivity of Composite Polyelectrolyte Membranes with Metal-Organic Frameworks for Fuel Cell Applications. *Adv. Mater. Interfaces* **2019**, *6*, 1801146. [CrossRef]

80. Sacco, A. Electrochemical impedance spectroscopy: Fundamentals and application in dye-sensitized solar cells. *Renew. Sustain. Energy Rev.* **2017**, *79*, 814–829. [CrossRef]

81. Barsoukov, J.R.E. *Macdonald, Impedance Spectroscopy: Theory, Experiment, and Applications*; John Wiley & Sons, Inc.: Hoboken, NJ, USA, 2005.

82. Jun, Y.S.; Um, J.G.; Jiang, G.; Lui, G.; Yu, A. Ultra-large sized graphene nano-platelets (GnPs) incorporated polypropylene (PP)/GnPs composites engineered by melt compounding and its thermal, mechanical, and electrical properties. *Compos. Part B Eng.* **2018**, *133*, 218–225. [CrossRef]

83. Vega-Moreno, J.; Lemus-Santana, A.A.; Reguera, E.; Andrio, A.; Compañ, V. High proton conductivity at low and moderate temperature in a simple family of Prussian blue analogs, divalent transition metal hexacyanocobaltates (III). *Electrochim. Acta* **2020**, *360*, 136959. [CrossRef]

84. Del Castillo, R.M.; del Castillo, L.F.; Alipio, G. Calles and Vicente Compañ Experimental and computational conductivity study of multilayer graphene in polypropylene nanocomposites. *J. Mater. Chem. C* **2018**, *6*, 7232. [CrossRef]

85. Sarjanović, J.; Stojić, M.; Rubčić, M.; Pavić, L.; Pisk, J. Impedance Spectroscopy as a Powerful Tool for Researching Molybdenum-Based Materials with Schiff Base Hydrazones. *Materials* **2023**, *16*, 1064. [CrossRef]

86. Lin, P.; Sun, X.-M. A Universal Interpretation of Three Types of Resonator-Based Controllers. *IEEE Trans. Circuits Syst. II Express Briefs* **2023**, *70*, 2555–2559. [CrossRef]

87. Dong, J.; Gong, C.; Bao, J.; Zhu, L.; Chen, H.; Wang, Z. Power Synchronization Compensation Strategy Based on Second-Order Compensation Links for Voltage-Controlled Inverters in Microgrids. *J. Mod. Power Syst. Clean Energy* **2023**. Online first articles.

88. García-Bernabé, A.; Rivera, A.; Granados, A.; Luis, S.V.; Compañ, V. Ionic transport on composite polymers containing covalently attached and absorbed ionic liquid fragments. *Electrochim. Acta* **2016**, *213*, 887–897. [CrossRef]

89. Andrio, A.; Hernández, S.I.; García-Alcántara, C.; del Castillo, L.F.; Compañ, V.; Santamaría-Holek, I. Temperature dependence of anomalous protonic and superprotonic transport properties in mixed salts based on CsH_2PO_4. *Phys. Chem. Chem. Phys.* **2019**, *21*, 12948. [CrossRef]

90. Fuentes, I.; Mostazo-López, M.J.; Kelemen, Z.; Compañ, V.; Andrio, A.; Morallón, E.; Cazorla-Amorós, D.; Viñas, C.; Teixidor, F. Are the Accompanying Cations of Doping Anions Influential in Conducting Organic Polymers? The Case of the Popular PEDOT. *Chem. Eur. J.* **2019**, *25*, 14308–14319. [CrossRef] [PubMed]

91. Prokhorov, Y.; Luna-Barcenas, G.; Kovalenko, Y. Interphase percolation phenomena in chitosan-graphene oxide nanocomposites, the role of water content. *Express Polym. Lett.* **2023**, *17*, 29–39. [CrossRef]

92. Chfii, H.; Bouich, A.; Soucase, B.M.; Abdlefdil, M. A new approach for growing high-quality delafossite $CuCoO_2$ films by spray pyrolysis through the optimization of the Cu/Co ratio. *Opt. Mater.* **2023**, *135*, 113229. [CrossRef]

93. Saber, S.; Marí, B.; Andrio, A.; Escorihuela, J.; Khattab, N.; Eid, A.; Nahrawy, A.; Aly, M.A.; Compañ, V. Structural and Electrochemical Analysis of CIGS: Cr Crystalline Nanopowders and Thin Films Deposited onto ITO Substrates. *Nanomaterials* **2021**, *11*, 1093. [CrossRef]

94. Jonscher, A.K. The 'universal' dielectric response. *Nature* **1977**, *267*, 673. [CrossRef]

95. Galindo, B.; Benedito, A.; Gimenez, E.; Compañ, V. Comparative study between the microwave heating efficiency of carbon nanotubes versus multilayer graphene in polypropylene nanocomposites. *Compos. Part B Eng.* **2016**, *98*, 330–338. [CrossRef]

96. Valverde, D.; Garcia-Bernabé, A.; Andrio, A.; García-Verdugo, E.; Luis, S.V.; Compañ, V. Free ion diffusivity and charge concentration on cross-linked polymeric ionic liquid iongel films based on sulfonated zwitterionic salts and lithium ions. *Phys. Chem. Chem. Phys.* **2019**, *21*, 17923–17932. [CrossRef]

97. Sidebottom, D.L. Dimensionality Dependence of the Conductivity Dispersion in Ionic Materials. *Phys. Rev. Lett.* **1999**, *83*, 983–986. [CrossRef]

98. Banerjee, P.; Pal, P.; Ghosh, A.; Mandal, T.K. Ion transport and relaxation in phosphonium poly(ionic liquid) homo- and co-polymers. *J. Polym. Sci.* **2021**, *59*, 1556–1570. [CrossRef]

99. Bouich, A.; Torres, J.C.; Chfii, H.; Marí-Guaita, J.; Khattak, Y.H.; Baig, F.; Soucase, B.M.; Palacios, P. Delafossite as hole transport layer a new pathway for efficient perovskite-based solar cells: Insight from experimental, DFT and numerical analysis. *Sol. Energy* **2023**, *250*, 18–32. [CrossRef]

100. Gilbert, T.L. Hohenberg-Kohn theorem for nonlocal external potentials. *Phys. Rev. B* **1975**, *12*, 2111–2120. [CrossRef]

101. Seidl, A.; Görling, A.; Vogl, P.; Majewski, J.A.; Levy, M. Generalized Kohn-Sham schemes and the band-gap problem. *Phys. Rev. B* **1996**, *53*, 3764–3774. [CrossRef] [PubMed]

102. Blöchl, P.E. Projector augmented-wave method. *Phys. Rev. B* **1994**, *50*, 17953–17979. [CrossRef] [PubMed]

103. Krukau, A.V.; Vydrov, O.A.; Izmaylov, A.F.; Scuseria, G.E. Influence of the Exchange Screening Parameter on the Performance of Screened Hybrid Functionals. *J. Chem. Phys.* **2006**, *125*, 224106. [CrossRef] [PubMed]

104. Heyd, J.; Scuseria, G.E.; Ernzerhof, M. Hybrid functionals based on a screened Coulomb potential. *J. Chem. Phys.* **2003**, *118*, 8207–8215. [CrossRef]

105. Heyd, J.; Scuseria, G.E. Assessment and validation of a screened Coulomb hybrid density functional. *J. Chem. Phys.* **2004**, *120*, 7274–7280. [CrossRef]

106. Kresse, G.; Hafner, J. Ab Initio Molecular Dynamics for Open-shell Transition Metals. *Phys. Rev. B* **1993**, *48*, 13115–13118. [CrossRef]

107. Kresse, G.; Furthmüller, J. Efficient Iterative Schemes for Ab Initio Total-Energy Calculations Using a Plane-Wave Basis Set. *Phys. Rev. B* **1996**, *54*, 11169–11186. [CrossRef] [PubMed]

108. Kresse, G.; Joubert, D. From ultrasoft pseudopotentials to the projector augmented-wave method. *Phys. Rev. B* **1999**, *59*, 1758–1775. [CrossRef]

109. Monkhorst, H.J.; Pack, J.D. Special points for Brillouin-zone integrations. *Phys. Rev. B* **1976**, *13*, 5188–5192. [CrossRef]

110. Chfii, H.; Bouich, A.; Soucase, B.M.; Abd-Lefdil, M. Structural and physical properties of Mg-doped $CuCoO_2$ delafossite thin films. *Mater. Chem. Phys.* **2023**, *306*, 128006. [CrossRef]

111. Bouich, A.; Torres, J.C.; Khattak, Y.H.; Baig, F.; Marí-Guaita, J.; Soucase, B.M.; Mendez-Blas, A.; Palacios, P. Bright Future by Controlling α/δ Phase Junction of Formamidinium Lead Iodide Doped by Imidazolium for Solar Cells: Insight from Experimental, DFT Calculations and SCAPS Simulation. *Surf. Interfaces* **2023**, *40*, 103159. [CrossRef]

112. Bouich, A.; Marí-Guaita, J.; Soucase, B.M.; Palacios, P. Bright future by enhancing the stability of methylammonium lead triiodide perovskites thin films through Rb, Cs and Li as dopants. *Mater. Res. Bull.* **2023**, *163*, 112213. [CrossRef]

113. Doumbia, Y.; Bouich, A.; Soucase, B.M.; Soro, D. Towards Stable Free Lead Mixed Halide Perovskite Thin Films on FTO-Coated Glass Substrate. *JOM* **2023**, 1–6. [CrossRef]
114. Brik, M.; Srivastava, A.; Popov, A. A few common misconceptions in the interpretation of experimental spectroscopic data. *Opt. Mater.* **2022**, *127*, 112276. [CrossRef]